Journal of Computational Physics 436 (2021) 110281

Contents lists available at ScienceDirect

Journal of Computational Physics

www.elsevier.com/locate/jcp

Conservative semi-Lagrangian schemes for kinetic equations Part II: Applications

Seung Yeon Cho [a,*], Sebastiano Boscarino [a], Giovanni Russo [a], Seok-Bae Yun [b]

[a] Department of Mathematics and Computer Science, University of Catania, Catania 95125, Italy
[b] Department of Mathematics, Sungkyunkwan University, Suwon 440-746, Republic of Korea

ARTICLE INFO

Article history:
Available online 16 March 2021

Keywords:
Conservative reconstruction
Semi-Lagrangian method
BGK model
Vlasov-Poisson system

ABSTRACT

In this paper, we present a new class of conservative semi-Lagrangian schemes for kinetic equations. They are based on the conservative reconstruction technique introduced in [1]. The methods are high order accurate both in space and time. Because of the semi-Lagrangian nature, the time step is not restricted by a CFL-type condition. Applications are presented to the Vlasov-Poisson system and the BGK model of rarefied gas dynamics. In the first case, operator splitting is adopted to obtain high order accuracy in time, and a conservative reconstruction that preserves the maximum and minimum of the function is used. For initially positive solutions, in particular, this guarantees exact preservation of the L^1-norm. Conservative schemes for the BGK model are constructed by coupling the conservative reconstruction with a conservative treatment of the collision term. High order in time is obtained by either Runge-Kutta or BDF time discretization of the equation along characteristics. Because of L-stability and exact conservation, the resulting scheme for the BGK model is *asymptotic preserving* for the underlying fluid dynamic limit. Several test cases in one and two space dimensions confirm the accuracy and robustness of the methods, and the AP property of the schemes when applied to the BGK model.

1. Introduction

In the first part of this paper [1], we introduce and analyse a new conservative reconstruction, which is now adopted to build conservative semi-Lagrangian (SL) schemes for various equations, including rigid rotation and kinetic equations. The basic idea of the semi-Lagrangian approach is to integrate the equations along the characteristics and update solutions on a fixed grid. This allows the use of larger time steps with respect to Eulerian methods, which suffer from CFL-type time step restrictions.

For this reason, SL methods are suitable for the numerical treatment of kinetic equations, where the collision term may be expensive, and they have been extensively adopted in the literature in the context of the Vlasov-Poisson model [2–4] or BGK-type models [5–7].

Since the aforementioned kinetic equations have various conservative quantities, the conservation property is very relevant in the numerical treatment of such models. In particular, it could be crucial to maintain conservation for the long time simulation of the Vlasov-Poisson equation or for capturing shocks correctly in the fluid limit of the BGK model.

* Corresponding author.
E-mail addresses: chosy89@skku.edu (S.Y. Cho), boscarino@dmi.unict.it (S. Boscarino), giovanni.russo1@unict.it (G. Russo), sbyun01@skku.edu (S.-B. Yun).

https://doi.org/10.1016/j.jcp.2021.110281
0021-9991/

On the other hand, the characteristic tracing structure of SL method necessarily requires to compute the numerical solutions on points which do not lay on a grid. Hence, it is important to take into account a reconstruction technique which gives high order accurate and conservative solutions. Also, it may be relevant to preserve other properties of the solution. For example, in the case of the initial value problem for the Vlasov-Poisson system, the distribution function is carried unchanged along particle trajectories, therefore the range of the solution (the interval between minimum and maximum of the initial condition) is maintained, so it would be nice to prevent the numerical solution from exceeding such a range at a discrete level. In other cases, e.g. for piecewise smooth solutions with jump discontinuities for the BGK model, it is important to prevent the appearance of spurious oscillations. All these properties crucially depend on the details of the reconstruction, not only on its conservation property.

High order non-oscillatory WENO type interpolations, such as the one introduced in [8], and that we call *generalized WENO* (GWENO), or the one used in [9], can be adopted, for example, to prevent the appearing of spurious oscillations. They have been applied to develop a class of non-splitting SL methods [5,10,11] developed for the BGK model [12] of the celebrated Boltzmann equation [13] of rarefied gas-dynamics. However, when numerical solutions contain discontinuities, such schemes may not be conservative due to the non-linear weights used for relieving oscillations [14].

As a remedy for the lack of conservation, several approaches introduce high-order conservative and non-oscillatory schemes [15,16]. In [17] the authors propose a slope correction to prevent negativity, which is further improved in [18].

In this paper, we use a technique of conservative reconstructions introduced in [1]. In particular, a maximum principle preserving (MPP) limiter [19,20] is adopted in order to preserve the range of the solution, while CWENO reconstructions [21–24] are taken as basic reconstructions to prevent appearing of spurious oscillations. A combination of CWENO and MPP limiter has been adopted in [25] in the context of Eulerian schemes. We explore here the use of this technique in the context of semi-Lagrangian schemes.

Three problems are considered in this paper, and each of them is solved by a high-order, conservative, semi-Lagrangian, finite-difference method. The detail of the method, however, depends on the problem.

As a warm up problem we consider rigid body rotation, for which a comparison with an exact solution is possible. High-order in time is obtained by operator splitting.

The second problem we deal with is the Vlasov-Poisson system in plasma dynamics. Since the system has various time-invariant quantities, conservation and positivity are very important and become more relevant for long time simulation. There is a vast literature on SL methods for the VP system. Among them, splitting methods [2,17,15,16] have been often adopted due to their simplicity in treating transport-type equations (see [4] for non-splitting methods).

To construct high-order schemes which maintain positivity and conservation, we combine our reconstruction to high-order splitting methods proposed in [26,27]. Note that in the multidimensional case we do not need to adopt dimensional splitting for transport-type equations (see Section 5.1).

In [14], we proposed a SL scheme based on a non-conservative predictor and a conservative corrector, which in conjunction with a discrete Maxwellian [28] produces a conservative scheme. Although the scheme allows large time steps for small collision times, a related stability analysis [14] shows severe stability restrictions on the time step, especially in the rarefied regime.

In this paper, we will return to the standard SL approach [5] and apply our conservative reconstruction, thus obtaining a conservative SL scheme which performs well in all range of Knudsen number with no CFL-type stability restrictions. Concerning convergence analysis on the semi-Lagrangian schemes for BGK-type models, we refer to [29–31].

The rest of this paper is organised as follows: In Section 2, we recall the two kinetic models of interest, namely the Vlasov-Poisson system of plasma physics and the BGK model of rarefied gas dynamics. In Section 3, we briefly recall the conservative reconstruction introduced in [1]. Section 4 is devoted to the construction of semi-Lagrangian schemes for specific applications, such as rigid rotation, Vlasov-Poisson system and BGK model. In Section 5, we describe high order splitting SL methods for the rigid rotation and the Vlasov-Poisson equations, and high order non-splitting SL schemes for the BGK model. In Section 7, we provide several numerical tests demonstrating the performance of our conservative reconstruction applied to the SL schemes. In the last section, we draw some conclusions.

2. Kinetic models

Here we consider two kinetic equations: the Vlasov-Poisson system and the BGK model.

2.1. Vlasov-Poisson system

In plasma physics, the motion of electrons forced by a self-consistent electric field is described by the Vlasov-Poisson system (see, for example, [32], Sec.6.14), which we write in nondimensional form as

$$\begin{aligned}
&\frac{\partial f}{\partial t} + v \cdot \nabla_x f + \mathbb{E}(x,t) \cdot \nabla_v f = 0 \\
&\mathbb{E}(x,t) = -\nabla_x \phi(x,t), \qquad -\Delta_x \phi(x,t) = \rho(x,t) - m, \\
&\rho(x,t) = \int_{\mathbb{R}^{d_v}} f(x,v,t)\, dv, \quad m = \frac{1}{L^{d_x}} \int_{\mathbb{T}^{d_x}} \int_{\mathbb{R}^{d_v}} f(x,v,t)\, dv\, dx.
\end{aligned} \tag{1}$$

Here $f(x,v,t)$ is the electron number density in phase space; $(x,v) \in \Omega := \mathbb{T}^{d_x} \times \mathbb{R}^{d_v}$ at time $t > 0$ where the space $\mathbb{T}^{d_x}$ and $\mathbb{R}^{d_v}$ denote the d_x-dimensional torus $\mathbb{R}^{d_x}/(L\mathbb{Z}^{d_x})$ and d_v-dimensional Euclidean space, respectively. $\mathbb{E}(x,t)$ denotes the electric field, and $\phi(x,t)$ is the self-consistent electrostatic potential. We use ρ to denote electron charge density and m the ion charge density assumed to be uniformly distributed on the background. Because ions are much heavier than electrons, as a first approximation one may assume they are fixed in space. Here we further assume their density is constant. It is common to assume that the system has global charge neutrality. Because of periodic boundary condition on the spatial domain, the integral of right hand side of Poisson equation in (1) w.r.t. x variable has to vanish.

In the system, the distribution function f satisfies the following properties:

1. Maximum principle:

$$0 \le f(x,v,t) \le M, \quad \forall t > 0, \quad (x,v) \in \Omega$$

   provided $0 \le f_0(x,v) \le M, \ (x,v) \in \Omega$.
2. Conservation of total mass:

$$\frac{d}{dt} \int_{\mathbb{R}^{d_v}} \int_{\mathbb{T}^{d_x}} f\, dx\, dv = 0.$$

3. Conservation of L^p norm $1 \le p < \infty$:

$$\|f\|_p = \left(\int_{\mathbb{R}^{d_v}} \int_{\mathbb{T}^{d_x}} |f|^p\, dx\, dv \right)^{1/p}.$$

4. Conservation of energy:

$$\text{Energy} = \int_{\mathbb{R}^{d_v}} \int_{\mathbb{T}^{d_x}} \frac{|v|^2}{2} f\, dx\, dv + \int_{\mathbb{T}^{d_x}} \frac{|\mathbb{E}|^2}{2}\, dx. \tag{2}$$

5. Conservation entropy:

$$\text{Entropy} = \int_{\mathbb{R}^{d_v}} \int_{\mathbb{T}^{d_x}} f \log \frac{1}{f}\, dx\, dv.$$

2.2. BGK model for the Boltzmann equation

The BGK model is a well-known approximation model for the Boltzmann equation of rarefied gas dynamics, based on the replacement of the collision integral of the Boltzmann equation with a relaxation operator. The BGK model reads:

$$\frac{\partial f}{\partial t} + v \cdot \nabla_x f = \frac{1}{\kappa} \left(\mathcal{M}(f) - f \right), \tag{3}$$

where $f(x,v,t)$ is the number density of monatomic particles on the phase space $\mathbb{R}^{d_x} \times \mathbb{R}^{d_v}$ at time $0 \le t \in \mathbb{R}_+$. Here $\mathbb{R}$ is the real number, and d_x and d_v denote the dimension for space and velocity variables, respectively. We consider a fixed non-dimensional collision frequency characterized by the Knudsen number $\kappa > 0$ representing the ratio between the mean free path of particle and the physical length scale under consideration. In (3), the collision integral of the Boltzmann equation is replaced with the relaxation process towards the local thermodynamical equilibrium, so called the local Maxwellian $\mathcal{M}(f)$:

$$\mathcal{M}(f)(x,v,t) := \frac{\rho(x,t)}{\sqrt{(2\pi T(x,t))^{d_v}}} \exp\left(-\frac{|v - U(x,t)|^2}{2T} \right). \tag{4}$$

Here macroscopic densities for mass ρ, momentum ρU, energy E and temperature T are defined by

$$\left(\rho,\ \rho U,\ 2E,\ d_v \rho T\right)^\top = \int_{\mathbb{R}^{d_v}} \left(1,\ v,\ |v|^2, |v-U|^2\right) f dv.$$

Note that the relaxation operator still maintains some qualitative features of the Boltzmann collision operator:

- Collision invariance $1, v, |v|^2$:

$$\int_{\mathbb{R}^{d_v}} (\mathcal{M}(f) - f) \begin{pmatrix} 1 \\ v \\ |v|^2 \end{pmatrix} dv = 0. \tag{5}$$

- Conservation laws for mass, momentum and energy:

$$\frac{d}{dt} \int_{\mathbb{R}^{d_x}\times\mathbb{R}^{d_v}} f\phi(v)\, dx dv = 0,$$

  where $\phi(v) := \left(1, v, \frac{|v|^2}{2}\right)^\top$.

- The H-theorem:

$$\frac{d}{dt} \int_{\mathbb{R}^{d_x}\times\mathbb{R}^{d_v}} f \log \frac{1}{f}\, dx dv \geq 0.$$

- In the fluid regime $\kappa \to 0$, the solution f tends to $\mathcal{M}$. Then, the macroscopic moments of f satisfy the compressible Euler system:

$$\begin{aligned} &\rho_t + \nabla_x \cdot (\rho u) = 0, \\ &(\rho u)_t + \nabla_x \cdot (\rho u \otimes u + \rho T I_d) = 0, \\ &E_t + \nabla_x \cdot [(E + \rho T)\, u] = 0, \end{aligned}$$

  where I_d denotes the identity matrix in d_x dimension.

3. Conservative reconstruction

Here we briefly summarize the one-dimensional conservative point-wise reconstruction introduced in [1]. Since extension to the two-dimensional case is straightforward, we refer to [1] for details.

Let us consider a uniform mesh of size Δx with grid points $x_i \equiv x_{min} + i\Delta x$, of the computational domain $[x_{min}, x_{max}]$. The set of all space indices will be denoted by $\mathcal{I}$. Suppose that $u(x) = \frac{1}{\Delta x}\int_{x-\Delta x/2}^{x-\Delta x/2} \hat{u}(y)dy$ is the function we want to reconstruct. The procedure for the conservative reconstruction is given as follows:

1. Given point-wise values $\{u_i\}_{i\in\mathcal{I}}$ for each $i \in \mathcal{I}$, we reconstruct a polynomial of even degree k:

$$R_i(x) = \sum_{\ell=0}^{k} \frac{R_i^{(\ell)}}{\ell!} (x - x_i)^\ell$$

   which has the following properties:
   - High order accurate in the approximation of smooth $\hat{u}(x)$ (see [1], Proposition 2.1):
     - If ℓ is an even integer such that $0 \leq \ell \leq k$,

$$\hat{u}_i^{(\ell)} = R_i^{(\ell)} + \mathcal{O}(\Delta x^{k+2-\ell}).$$

     - If ℓ is an odd integer such that $0 \leq \ell < k$,

$$\hat{u}_i^{(\ell)} - \hat{u}_{i+1}^{(\ell)} = R_i^{(\ell)} - R_{i+1}^{(\ell)} + \mathcal{O}(\Delta x^{k+2-\ell}).$$

   - Essentially non-oscillatory.
   - Positivity preserving.
   - Conservative in the sense of cell averages:

$$\frac{1}{\Delta x} \int_{x_{i-\frac{1}{2}}}^{x_{i+\frac{1}{2}}} R_i(x)\, dx = u_i.$$

2. Using the obtained values $R_i^{(\ell)}$ for $0 \le \ell \le k$, we approximate $u(x_{i+\theta})$, $\theta \in [0,1)$, to $O(\Delta x^{k+2})$ with

$$Q(x_i + \theta\Delta x) = \sum_{\ell=0}^{k} (\Delta x)^\ell \left(\alpha_\ell(\theta) R_i^{(\ell)} + \beta_\ell(\theta) R_{i+1}^{(\ell)} \right),$$

where $\alpha_\ell(\theta)$ and $\beta_\ell(\theta)$ are given by

$$\alpha_\ell(\theta) = \frac{1-(2\theta-1)^{\ell+1}}{2^{\ell+1}(\ell+1)!}, \quad \beta_\ell(\theta) = \frac{(2\theta-1)^{\ell+1}-(-1)^{\ell+1}}{2^{\ell+1}(\ell+1)!}$$

for $\theta \in [0,1)$.

In [1], we adopt CWENO reconstructions as basic reconstructions $R_i(x)$, which leads to high order conservative non-oscillatory reconstruction. Here, we can further impose the maximum principle preserving property on $Q(x)$ by using a linear scaling technique [19,20,25].

The procedure works as follows: we first compute the linear scaling parameter in cell i:

$$\xi_i = \max\left\{1, \frac{|M-u_i|}{|M_i'-u_i|}, \frac{|m-u_i|}{|m_i'-u_i|}\right\}, \tag{6}$$

where M and m are maximum and minimum values of a known function u on the whole computational domain, and M_i' and m_i' are maximum and minimum values of local reconstruction $R_i(x)$ on the cell I_i. Next, we use ξ_i to CWENO reconstructions $R_i(x)$ as follows:

$$\tilde{R}_i(x) = u_i + \xi_i(R_i(x) - u_i),$$

where $\tilde{R}_i(x)$ is the rescaled polynomial defined on I_i::

$$\tilde{R}_i(x) = \sum_{\ell=0}^{k} \frac{\tilde{R}_i^{(\ell)}}{\ell!}(x-x_i)^\ell$$

Consequently,

$$\tilde{R}_i^{(0)} = u_i + \xi_i(R_i^{(0)} - u_i), \quad \tilde{R}_i^{(\ell)} = \xi_i R_i^{(\ell)}, \quad 1 \le \ell \le k,$$

from which we obtain a positive reconstruction $Q(x_i + \theta\Delta x)$:

$$Q(x_i + \theta\Delta x) = \sum_{\ell=0}^{k} (\Delta x)^\ell \left(\alpha_\ell(\theta) \tilde{R}_i^{(\ell)} + \beta_\ell(\theta) \tilde{R}_{i+1}^{(\ell)} \right).$$

We remark that the maximum preserving property still holds for $Q(x)$, $\forall x$, because $Q(x)$ is obtained by taking the sliding average of a piecewise reconstruction satisfying the maximum preserving property:

$$m \le Q(x) = \frac{1}{\Delta x} \int_{x-\Delta x/2}^{x+\Delta x/2} R(y)\,dy \le M.$$

In some applications like the Vlasov-Poisson model, it is not necessary to impose the non-oscillatory property. In this case, $R_i(x)$ will be polynomials interpolating u_i in terms of cell average, i.e. the CWENO polynomial with *linear weights*.

Note that the limiter can be useful if we have some preliminary information about the maximum M and minimum m values of the exact solution to problems of interest. For example, in the case of the advection equation or rigid body rotation, the range of the solution is determined by initial data. Similarly, the Vlasov-Poisson model is known to have such bound since the function is carried unchanged along the characteristic.

4. Semi-Lagrangian methods

A semi-Lagrangian method can be obtained by integrating the equation of interest along its characteristic curves. As the simplest case, we consider a one-dimensional transport equation:

$$\partial_t f + a\partial_x f = 0, \quad t \ge 0,\ x \in \mathbb{R}, \tag{7}$$

where a is a fixed constant in $\mathbb{R}$. Let us denote the n-th time step by $t^n := n\Delta t$, $n \in \mathbb{N}$ for $\Delta t > 0$. Given the distribution function f at time t^n, the exact solution on x_i at t^{n+1} is given by

$$f(x_i, t^{n+1}) = f(X(t^n; x_i, t^{n+1}), t^n),$$

where $X(t; x_i, t^{n+1})$ satisfies

$$\frac{dX}{dt} = a, \quad X(t^{n+1}) = x_i,$$

therefore, $X(t^n; x_i, t^{n+1}) = x_i - a\Delta t$.

Considering that the characteristic foot $x_i - a\Delta t$ can be located on off-grid points, one can update solutions after reconstructing $f(x_i - a\Delta t, t^n)$ from given solutions on grid points. For the semi-Lagrangian schemes proposed in this paper, we will use the conservative reconstruction described in section 3.

In the following we will discuss the application of semi-Lagrangian methods to a basic test problem: *the rigid body rotation* and to two kinetic equations: *the Vlasov-Poisson system* and *the BGK model*.

For simplicity, in this paper we deal only with periodic or free-flow BC's in space. Other boundary conditions for SL methods applied to the BGK model have been treated, for example, in [33,34].

4.1. Semi-Lagrangian methods for the rigid body rotation

Rigid body rotation of objects can be described by a linear model:

$$u_t - yu_x + xu_y = 0, \quad (x, y) \in \mathbb{R}^2. \tag{8}$$

One can design a semi-Lagrangian method using the information that the solution is constant along the characteristic curves

$$(X(t), Y(t)) \equiv \left(X(t; x, y, t^{n+1}), Y(t; x, y, t^{n+1})\right)$$

satisfying

$$\frac{dX}{dt} = -Y, \quad \frac{dY}{dt} = X, \quad X(t^{n+1}) = x, \quad Y(t^{n+1}) = y.$$

In this case the backward characteristics can be solved exactly as

$$X(t^n) = x\cos(\Delta t) + y\sin(\Delta t), \quad Y(t^n) = -x\sin(\Delta t) + y\cos(\Delta t), \tag{9}$$

so that

$$u(x, y, t^{n+1}) = u(X(t^n), Y(t^n), t^n).$$

Notice that, when computed on a grid, such exact solution is not strictly conservative, in the sense that the discrete sum of the solution is not equal to the discrete sum of the initial condition on the same grid. Here we shall not make use of the exact trajectories, which are often difficult to compute.

A general way to construct conservative schemes is based on splitting methods. A brief introduction of splitting methods is postponed to the Section 5.1.

The exact solution to Eq. (8) is obtained by rotating the initial data. When solving (8) numerically, one would like to preserve the qualitative structure of the solution such as, for example, its maximum and minimum values or any discontinuity, while preventing spurious oscillation. For these reasons, we will adopt QCWENO reconstructions which includes MPP limiter (6) for solving Eq. (8). Numerical examples are reported in Section 6.1.

4.2. Semi-Lagrangian methods for the Vlasov-Poisson system

Following the notation of Sect. 4, we set $a \equiv (v, \mathbb{E}(t, x, v))$ and $\nabla \equiv (\nabla_x, \nabla_v)$. Then we can rewrite (1) in the form (7). If a is sufficiently smooth (Lipschitz continuous), we can define unique characteristic curves of the first order differential operator,

$$\frac{\partial}{\partial t} + a \cdot \nabla,$$

which solve the following system

$$\begin{aligned} &\frac{dX}{dt}(t; x, v, t^{n+1}) = V(t; x, v, t^{n+1}), \\ &\frac{dV}{dt}(t; x, v, t^{n+1}) = \mathbb{E}(t, X(t; x, v, t^{n+1})). \end{aligned} \tag{10}$$

Here we denote by $(X(t; x, v, t^{n+1}), V(t; x, v, t^{n+1}))$ a characteristic curve which takes the value (x, v) at time t^{n+1}. Since the distribution function of the VP system is constant along the particle trajectories, we have

$$f(x, v, t^{n+1}) = f(X(t^n; x, v, t^{n+1}), V(t^n; x, v, t^{n+1})).$$

To update the solution in this way one has to perform a shift in both space and velocity. By adopting a splitting approach, a combination of separate shifts in the x and v direction is performed. The shift along the x-axis requires to solve a transport equation with velocity v, while the shift along the v-axis requires to solve a transport equation with electric field $\mathbb{E}$, which in turn is obtained by the solution of the Poisson equation for the potential in (1).

High-order time splitting methods used for VP system in the numerical tests are listed in Sect. 5.1.

Hereafter, let us denote velocity grids by $v_j = v_{min} + (j-1)\Delta v$ with mesh size $\Delta v > 0$ and the set of indices j by $\mathcal{J}$. This notation will be also used for the description of numerical methods for the BGK model. In (1), considering that $\mathbb{E} = -\nabla_x \phi$, one should find the potential function ϕ_i^n in advance. For this, we solve the Poisson equation $-\Delta_x \phi = \rho - m$ in (1) with a Fast Fourier Transform using $\{\rho_i^n\}_{i\in\mathcal{I}}$ and m^n obtained by the midpoint rule:

$$\rho_i^n = \sum_j f_{i,j}^n (\Delta v)^{d_v}, \quad m^n = \frac{1}{L^{d_x}} \sum_{i,j} f_{i,j}^n (\Delta x)^{d_x} (\Delta v)^{d_v}. \tag{11}$$

We remark that the initial value of m^n is constant in time, thanks to the conservation property of the schemes, $m^n = m^0$. In one space dimension, we calculate the discrete electric field $E_i^n = -\partial_x \phi\big|_{(x,t)}$ as follows:

- 4th order approximation

$$\partial_x \phi\big|_{(x,t)=(x_i,t^n)} = \frac{8(\phi_{i+1}^n - \phi_{i-1}^n) - (\phi_{i+2}^n - \phi_{i-2}^n)}{12\Delta x} + \mathcal{O}\left((\Delta x)^4\right). \tag{12}$$

- 6th order approximation

$$\partial_x \phi\big|_{(x,t)=(x_i,t^n)} = \frac{45(\phi_{i+1}^n - \phi_{i-1}^n) - 9(\phi_{i+2}^n - \phi_{i-2}^n) + (\phi_{i+3}^n - \phi_{i-3}^n)}{60\Delta x} + \mathcal{O}\left((\Delta x)^6\right). \tag{13}$$

- 8th order approximation

$$\partial_x \phi\big|_{(x,t)=(x_i,t^n)} = \frac{672(\phi_{i+1}^n - \phi_{i-1}^n) - 168(\phi_{i+2}^n - \phi_{i-2}^n) + 32(\phi_{i+3}^n - \phi_{i-3}^n) - 3(\phi_{i+4}^n - \phi_{i-4}^n)}{840\Delta x} + \mathcal{O}\left((\Delta x)^8\right). \tag{14}$$

The approximation of $\nabla_x \phi$ in multi-dimension can be done by dimension-wise computation.

Remark 4.1. Considering the maximum principle of the Vlasov-Poisson system, it is natural to adopt a basic reconstruction which maintains the maximum and minimum of initial data together with conservation property. For these reasons, we use the MPP limiter (6) on polynomial interpolation in the sense of cell average.

4.3. A semi-Lagrangian method for the BGK model

Here, we review a class of non-splitting implicit semi-Lagrangian methods for the BGK model [5,10]. Note that we will apply the conservative reconstruction in Section 3 to the reconstruction of distribution on off-grid points.

4.3.1. First order semi-Lagrangian method for the BGK model

A first order SL method for the BGK model (3) is obtained by applying implicit Euler method to its characteristic form:

$$f_{i,j}^{n+1} = \tilde{f}_{i,j}^n + \frac{\Delta t}{\kappa}\left(\mathcal{M}[f_i^{n+1}]_j - f_{i,j}^{n+1}\right), \tag{15}$$

where $\tilde{f}_{i,j}^n$ is an approximation of $f(x_i - v_j \Delta t, v_j, t^n)$ which can be reconstructed from $\{f_{i,j}^n\}_{i\in\mathcal{I}}$. The quantity $\mathcal{M}[f_i^{n+1}]_j$ is the local Maxwellian computed by

$$\mathcal{M}[f_i^{n+1}]_j = \frac{\rho_i^{n+1}}{\sqrt{\left(2\pi T_i^{n+1}\right)^2}} \exp\left(-\frac{|v_j - U_i^{n+1}|^2}{2T_i^{n+1}}\right), \tag{16}$$

with discrete macroscopic quantities:

$$\left(\rho_i^{n+1},\ \rho_i^{n+1} U_i^{n+1},\ d_v \rho_i^{n+1} T_i^{n+1}\right) := \sum_{j\in\mathcal{J}} f_{i,j}^{n+1} \left(1, v_j, \left|v_j - U_i^{n+1}\right|^2\right) (\Delta v)^{d_v}. \tag{17}$$

Using the structural feature of the relaxation term of (3), one can compute (15) explicitly. Multiplying the collision invariant $\phi_j := (1, v_j, \frac{|v_j|^2}{2})$ to both sides of (15) and taking summation over $j \in \mathcal{J}$, one obtains

$$\sum_{j\in\mathcal{J}} \left(f_{i,j}^{n+1} - \tilde{f}_{i,j}^{n}\right)\phi_j(\Delta v)^{d_v} = \frac{\Delta t}{\kappa}\sum_{j\in\mathcal{J}} \left(\mathcal{M}[f_i^{n+1}]_j - f_{i,j}^{n+1}\right)\phi_j(\Delta v)^{d_v}. \tag{18}$$

Here the right hand side can be negligible if the discrete summation is computed with a sufficiently refined grid on the appropriate velocity domain, because midpoint rule is spectrally accurate when applied to a Maxwellian. Then, the discrete macroscopic quantities ρ_i^n, U_i^n and T_i^n can be computed as follows:

$$\left(\rho_i^{n+1},\, \rho_i^{n+1}U_i^{n+1},\, E_i^{n+1}\right) = \sum_{j\in\mathcal{J}} f_{i,j}^{n+1}\phi_j(\Delta v)^{d_v} = \sum_{j\in\mathcal{J}} \tilde{f}_{i,j}^{n}\phi_j(\Delta v)^{d_v} =: \left(\tilde{\rho}_i^{n+1},\, \tilde{\rho}_i^{n+1}\tilde{U}_i^{n+1},\, \tilde{E}_i^{n+1}\right), \tag{19}$$

this further gives

$$d_v\rho_i^{n+1}T_i^{n+1} = \sum_{j\in\mathcal{J}} f_{i,j}^{n+1}\left|v_j - U_i^{n+1}\right|^2(\Delta v)^{d_v} = \sum_{j\in\mathcal{J}} \tilde{f}_{i,j}^{n}\left|v_j - \tilde{U}_i^{n+1}\right|^2(\Delta v)^{d_v} = d_v\tilde{\rho}_i^{n+1}\tilde{T}_i^{n+1}. \tag{20}$$

Consequently, one can update solution as follows:

$$f_{i,j}^{n+1} = \tilde{f}_{i,j}^{n} + \frac{\Delta t}{\kappa}\left(\mathcal{M}[\tilde{f}_i^{n}]_j - f_{i,j}^{n+1}\right), \tag{21}$$

with

$$\mathcal{M}[\tilde{f}_i^{n}]_j = \frac{\tilde{\rho}_i^{n}}{\sqrt{\left(2\pi\tilde{T}_i^{n}\right)^{d_v}}}\exp\left(-\frac{|v_j - \tilde{U}_i^{n}|^2}{2\tilde{T}_i^{n}}\right).$$

4.3.2. Conservative approximation of Maxwellian

The treatment of the collision term as described in the previous section does not produce a strictly conservative method. Besides unavoidable round-off errors, there are two reasons for lack of strict conservation. The first one is the fact that the unbounded domain in velocity is truncated by a finite computational domain. The second one is that the moments $(\rho, \rho u, E)$ of the continuous Maxwellian (4) are exact only if computed by integration over v. If we compute the moments of the Maxwellian (16) by the discrete summation (17), there is a small discrepancy which is essentially due to the approximation of an integral by a discrete sum. The first source of error can be reduced by using a large enough computational domain in velocity, which essentially includes the numerical support of the distribution function. The second source of error can be reduced by using a relatively large number of grid points in velocity domain. Because classical midpoint rule is spectrally accurate when applied to a rapidly decreasing smooth function such as a Maxwellian, even a moderate number of grid points in velocity is usually sufficient to make conservation errors very small. However, for small Knudsen number the behaviour of the gas should be adequately described by a relatively small number of velocities. In such a case, the conservation error introduced by the use of a continuous Maxwellian may be relevant. Here we adopt two techniques which restore full conservation in the approximation of the moments.

L^2 minimization (dM_1). This technique has been introduced by Irene Gamba and coworkers in [35]. Let us define the discrete moments obtained by function $\tilde{f}$ by $\mathcal{U} := (\rho, \rho U, E)^\top \in \mathbb{R}^{d_v+2}$. The continuous Maxwellian with continuous moments equal to $\mathcal{U}$ will not have the same discrete moments of $\tilde{f}$. Therefore we define a new discrete Maxwellian $g = \{g_j\}_{j\in\mathcal{J}}$ by imposing that it is as close as possible to $\mathcal{M}[\mathcal{U}](v_j)$, and has exactly the same discrete moments $\mathcal{U}$. Let us consider d_v-dimensional velocity domain with grid points v_j for $j \in \mathcal{J}$. Then we solve the following minimization problem:

$$\min \left\|\mathcal{M} - g\right\|_2^2 \quad \text{s.t} \quad Cg = \mathcal{U} \tag{22}$$

where

$$\mathcal{M} \equiv (\mathcal{M}_1, \mathcal{M}_2, \cdots, \mathcal{M}_{(N_v+1)^{d_v}})^\top \in \mathbb{R}^{(N_v+1)^{d_v}}, \quad g = (g_1, g_2, \cdots, g_{(N_v+1)^{d_v}})^\top \in \mathbb{R}^{(N_v+1)^{d_v}}.$$

$$C := \begin{pmatrix} (\Delta v)^{d_v} \\ v_j(\Delta v)^{d_v} \\ \frac{|v_j|^2}{2}(\Delta v)^{d_v} \end{pmatrix} \in \mathbb{R}^{(d_v+2)\times(N_v+1)^{d_v}}, \quad \mathcal{U} = (\rho, \rho U, E)^\top \in \mathbb{R}^{(d_v+2)\times 1}.$$

$$\mathcal{M}_j \equiv \mathcal{M}[\mathcal{U}](v_j) := \frac{\rho}{\sqrt{(2\pi T)^{d_v}}}\exp\left(-\frac{\left|v_j - U\right|^2}{2T}\right), \quad j \in \mathcal{J},$$

where $d_v \rho T = 2E - \rho |U|^2$.

To solve the minimization problem (22), we use the method of Lagrange multiplier with the following Lagrangian $\mathcal{L}(g, \lambda)$:

$$\mathcal{L}(g, \lambda) = \left\| \mathcal{M} - g \right\|_2^2 + \lambda^\top (Cg - \mathcal{U}).$$

We first compute the gradient of $\mathcal{L}$ with respect to g and λ:

$$\begin{aligned} \nabla_g \mathcal{L} = 0 &\Leftrightarrow \quad g = \mathcal{M} + \tfrac{1}{2} C^\top \lambda \\ \nabla_\lambda \mathcal{L} = 0 &\Leftrightarrow \; Cg = \mathcal{U}. \end{aligned}$$

Then, we use these to derive

$$\begin{aligned} Cg = C\mathcal{M} + \frac{1}{2} CC^\top \lambda &\Leftrightarrow \mathcal{U} = C\mathcal{M} + \frac{1}{2} CC^\top \lambda \\ &\Leftrightarrow \lambda = 2(CC^\top)^{-1}(\mathcal{U} - C\mathcal{M}). \end{aligned}$$

Note that the matrix $CC^\top$ is invertible because it is symmetric and positive definite. Consequently,

$$g = \mathcal{M} + C^\top (CC^\top)^{-1} (\mathcal{U} - C\mathcal{M}). \tag{23}$$

Once the matrix $C^\top (CC^\top)^{-1}$ is computed, it can be stored and reused for other Maxwellian computations. In view of this, the minimization approach (22) only requires additional matrix computations in determining g.

Note that this technique does not necessarily preserve positivity of the solution.

Discrete Maxwellian (Entropy minimization, dM2). The second approach, introduced by Mieussens [28], determines the value of g by solving the following entropy minimization problem:

$$\min \left\{ \sum_{j \in \mathcal{J}} g_j \log g_j, \; g_j \geq 0 \quad \text{s.t.} \quad \sum_{j \in \mathcal{J}} g_j \phi_j (\Delta v)^{d_v} = \mathcal{U} \right\} \tag{24}$$

which is equivalent to solving the following equation:

$$\sum_{j \in \mathcal{J}} \left(\exp(a \cdot \phi_j) \right) \phi_j (\Delta v)^{d_v} = \mathcal{U} \quad \text{where} \quad a \in \mathbb{R}^{d_v + 2}. \tag{25}$$

Then, the solution $a \in \mathbb{R}^{d_v+2}$ of (25) gives the solution to (24):

$$g_j = \exp(a \cdot \phi_j) \text{ for } j \in \mathcal{J}. \tag{26}$$

Compared to the first method (23), this one may be more expensive in that it requires an iterative solution of the non-linear system (25), say by Newton's methods. However, this approach always gives non-negative Maxwellian, therefore it is more helpful in preserving positivity of the numerical solution of the BGK model (3).

Alternative techniques to preserve the moments are possible. For example in [36] the authors use a different correction previously introduced by Aristov and Tcheremissine [37].

5. High order time discretization

In this section we present high order integrators for the time discretization that we use in our numerical tests. In the context of semi-Lagrangian methods for rigid body rotation (8), we adopt splitting methods for which it is easier to impose positivity and conservation. For VP system, it is difficult to design high order non-splitting characteristic tracing method. In particular, when solving two-dimensional problems ($d_x = d_v = 2$), the feet of the characteristics are not located on a regular grid, and it is not obvious how to construct conservative schemes.

On the other hand, in splitting schemes conservation can be attained easily because characteristic curves are given by straight lines. It is straightforward to extend the idea of splitting to two-dimensional problems.

For the BGK model we consider diagonally implicit RK method and BDF multistep methods [38] for the treatment of stiffness arising for small Knudsen numbers.

5.1. High-order splitting methods

We consider an arbitrary system $\dot{y} = f_1(y) + f_2(y)$ in $\mathbb{R}^n$. The idea of splitting methods is to decompose this system into two parts: $\dot{y} = f_1(y)$ and $\dot{y} = f_2(y)$, and compute solutions of the two systems successively to yield a solution to the original system. For more details on splitting methods, we refer to [39]. Now, we apply the idea of splitting methods in the framework of semi-Lagrangian methods for the rigid body rotation (8) and VP system (1).

High-order splitting methods for rigid body rotation

In splitting methods for (8), we solve two problems in sequence:

$$u_t - yu_x = 0, \quad u_t + xu_y = 0. \tag{27}$$

Each problem can be dealt with as in the linear transport equation case (7). The solution to first equation from time t to time $t+\tau$ is written explicitly as

$$u(x, y, t+\tau) = e^{\tau\mathcal{X}} u(x, y, t) = u(x + y\tau, y, t),$$

while the solution to second equation is given by

$$u(x, y, t+\tau) = e^{\tau\mathcal{Y}} u(x, y, t) = u(x, y - x\tau, t),$$

where we denoted by $e^{\tau\mathcal{X}}$ and $e^{\tau\mathcal{Y}}$ respectively the operators representing a shift along the x-axis by an amount $-y\tau$, and a shift along then y-axis by an amount $x\tau$. Using such operators it is easy to construct splitting methods of various orders, that allow to compute $u^{n+1} \approx u(t^{n+1})$ from $u^n \approx u(t^n)$, as described in [27]. Here we illustrate the methods of order 2, 4 and 6 that are used in the present paper.

- 2nd order Strang splitting method:
  1. Shift along y-axis: $u^* = e^{\frac{\Delta t}{2}\mathcal{Y}} u^n$.
  2. Shift along x-axis: $u^{**} = e^{\Delta t\mathcal{X}} u^*$.
  3. Shift along y-axis: $u^{n+1} = e^{\frac{\Delta t}{2}\mathcal{Y}} u^{**}$.

  We can write this compactly as
  $$u^{n+1} = \mathcal{S}_2^{\Delta t} u^n := e^{\frac{\Delta t}{2}\mathcal{Y}} e^{\Delta t\mathcal{X}} e^{\frac{\Delta t}{2}\mathcal{Y}} u^n. \tag{28}$$
- 4th order splitting method [27]:
  $$u^{n+1} = \mathcal{S}_4^{\Delta t} u^n := \mathcal{S}_2^{x_1\Delta t} \mathcal{S}_2^{x_0\Delta t} \mathcal{S}_2^{x_1\Delta t} u^n, \tag{29}$$
  where $x_0 = -\frac{2^{1/3}}{2-2^{1/3}}$, $x_1 = \frac{1}{2-2^{1/3}}$.
- 6th order splitting method [27]:
  $$u^{n+1} = \mathcal{S}_6^{\Delta t} u^n := \mathcal{S}_4^{y_1\Delta t} \mathcal{S}_4^{y_0\Delta t} \mathcal{S}_4^{y_1\Delta t} u^n, \tag{30}$$
  where $y_0 = -\frac{2^{1/5}}{2-2^{1/5}}$, $y_1 = \frac{1}{2-2^{1/5}}$.

High-order splitting methods for VP system

Splitting methods to VP system (1) are based on solving separately the two equations:

$$\frac{\partial f}{\partial t} + v \cdot \nabla_x f = 0 \qquad \text{transport in space,} \tag{31}$$

$$\frac{\partial f}{\partial t} + \mathbb{E}(x,t) \cdot \nabla_v f = 0 \qquad \text{drift in velocity.} \tag{32}$$

Each equation can be solved along the characteristics, just as in the case of the rigid rotation.

- Transport step over a time step $\tau > 0$:
  $$f(x, v, t+\tau) = e^{\tau\mathcal{T}} f(x, v, t) = f(x - v\tau, v, t).$$
- Drift step over a time step $\tau > 0$.
  $$f(x, v, t+\tau) = e^{\tau\mathcal{U}} f(x, v, t) = f(x, v - \mathbb{E}(x,t)\tau, t).$$
  Here we can compute the electric field $\mathbb{E}(x,t)$ using $\{f(t)\}$. Depending on the desired accuracy in space, we will use one of (12), (13) or (14).

Note that both families of characteristic curves are given by straight lines, which enables one to compute the location of the foot of the characteristic analytically.

The extension to high order methods for VP system is straightforward. For second and fourth order splitting methods, we will use (28) and (29), respectively. To attain sixth order in time, we use a 11-stage splitting method constructed in [26],

Table 1
Coefficients in (33).

	$i=1$	$i=2$	$i=3$
a_i	0.16873595056343742244819 6	0.37785158922092830388076 6	−0.09317507956873145265792 4
b_i	0.04908646097611624549144 1	0.26417760988897670020014 6	0.18673592913490705430841 3
c_i	−0.00006972871505530508409 9	−0.00062570482743004718916 9	−0.00221308512404532556163 6
d_i	0	$-2.91660045768984781644569\,1\cdot 10^{-6}$	$3.04848026170003878868072\,3\cdot 10^{-5}$
e_i	0	0	$4.98554938787506812159398\,8\cdot 10^{-7}$

because it is more efficient than the 18-th stage sixth order schemes [27]. Let us denote the solution f at time t^n by f^n. Then, the 6th order 11-stage splitting method in [26] can be described as follows:

$$f^{n+1}=\psi_6^{\Delta t} f^n := e^{\Delta t\mathcal{D}_1}e^{a_1\Delta t\mathcal{T}}e^{\Delta t\mathcal{D}_2}e^{a_2\Delta t\mathcal{T}}e^{\Delta t\mathcal{D}_3}e^{a_3\Delta t\mathcal{T}}e^{\Delta t\mathcal{D}_3}e^{a_2\Delta t\mathcal{T}}e^{\Delta t\mathcal{D}_2}e^{a_1\Delta t\mathcal{T}}e^{\Delta t\mathcal{D}_1}f^n, \tag{33}$$

where $\mathcal{D}_i=(b_i+2c_im(\Delta t)^2+4d_im^2(\Delta t)^4-8e_im^3(\Delta t)^6)\mathcal{U}$, $i=1,2,3$. The value of m is computable as in (11), and the coefficients in D_i are given in Table 1.

5.2. High-order Runge-Kutta methods for the BGK model

In [5,10], considering the stiffness arising in the fluid limit $\kappa\to 0$ of the BGK model (3), high order semi-Lagrangian methods are obtained by combining high order L-stable diagonally implicit Runge-Kutta methods (DIRK) or backward-difference formulas (BDF) with high order spatial reconstructions. In this paper, we consider s-stage, L-stable diagonally implicit Runge-Kutta (DIRK) schemes [40], represented by the Butcher's table:

$$\begin{array}{c|c} c & A \\ \hline & b^\top \end{array}$$

where $A=[a_{ij}]$ is a $s\times s$ matrix such that $a_{ij}=0$ for $i<j$, $c=(c_1,\dots,c_s)^\top$ and $b=(b_1,\dots,b_s)^\top$ are coefficients vectors.

In the description of s-stage DIRK method, we use the following notation:

- The location of the characteristic foot on the ℓ-th stage along the k-th backward-characteristic starting from x_i with velocity v_j at time $t^n+c_k\Delta t$:

$$x_{i,j}^{k,\ell} := x_i-(c_k-c_\ell)v_j\Delta t$$

- The interpolation of the distribution function f on $x_{i,j}^{k,\ell}$:

$$F_{i,j}^{(k,\ell)} := \hat{f}(x_{i,j}^{k,\ell},v_j,t^n+c_\ell\Delta t).$$

  Setting $c_0=0$, we define

$$F_{i,j}^{(k,0)} := \hat{f}(x_i-v_jc_k\Delta t,v_j,t^n).$$

- RK fluxes:

$$K(x,v,t)=\frac{1}{\kappa}\left(\mathcal{M}(x,v,t)-f(x,v,t)\right)$$

  and its discrete values on $x_{i,j}^{k,\ell}$

$$K_{i,j}^{(k,\ell)}=\hat{K}(x_{i,j}^{k,\ell},v_j,t^n+c_\ell\Delta t),$$

where we denoted by $\hat{f}$ the interpolation of the distribution function f on the foot of the characteristic.

We summarize the scheme as follows:

Algorithm for s-order DIRK based methods

For $k=1,\dots,s$,

1. Interpolate $F_{i,j}^{(k,0)}$ on $x_{i,j}^{k,0}$ from $\{F_{i,j}^{(k,0)}\}_{i\in\mathcal{I}}$.
2. For $\ell=1\dots,k-1$, interpolate $K_{i,j}^{(k,\ell)}$ on $x_{i,j}^{k,\ell}$ from $\{K_{i,j}^{(\ell,\ell)}\}_{i\in\mathcal{I}}$. (Skip for $k=1$)

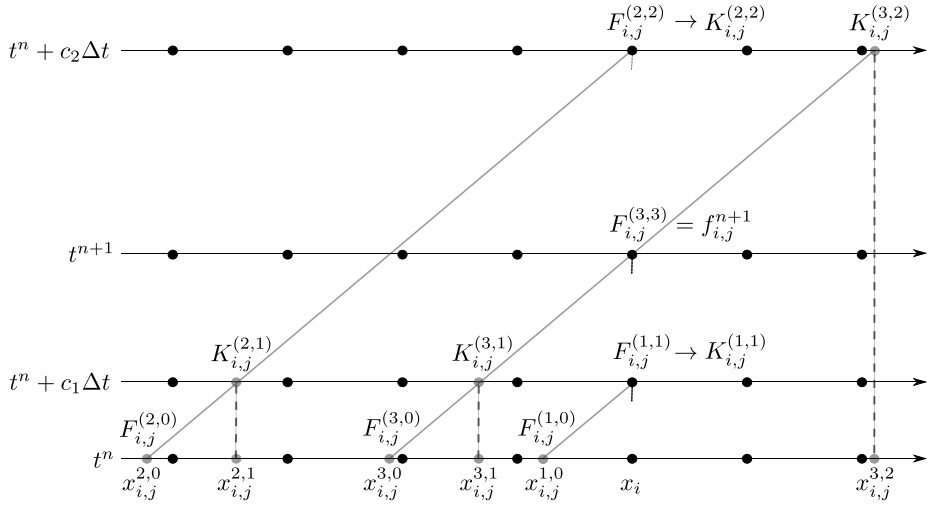

Fig. 1. Representation of DIRK3 scheme. Black circles: grid nodes, grey circles: points where interpolation is needed.

3. Compute:

$$F_{i,j}^{(k,k)} = F_{i,j}^{(k,0)} + \Delta t \sum_{\ell=1}^{k-1} a_{k\ell} K_{i,j}^{(k,\ell)} + \frac{\Delta t}{\kappa} a_{kk} \left(\mathcal{M}\left[F_i^{(k,k)}\right]_j - F_{i,j}^{(k,k)} \right), \tag{34}$$

where we compute the macroscopic moments of $\mathcal{M}\left[F_i^{(k,k)}\right]_j$ from $\left\{F_{i,j}^{(k,0)} + \Delta t \sum_{\ell=1}^{k-1} a_{k\ell} K_{i,j}^{(k,\ell)}\right\}_{j\in\mathcal{J}}$.

Due to the property that the adopted DIRK methods are stiffly accurate (SA), one can update solutions by setting $f_{i,j}^{n+1} = F_{i,j}^{(s,s)}$.

In our numerical tests, we use the third order L-stable DIRK (DIRK3) scheme introduced in [14]. The corresponding Butcher's table is

$$\begin{array}{c|cccc} \gamma & \gamma & 0 & 0 \\ c_2 & c_2-\gamma_2 & \gamma_2 & 0 \\ 1 & 1-b_2-\gamma & b_2 & \gamma \\ \hline & 1-b_2-\gamma & b_2 & \gamma_3 \end{array} \tag{35}$$

where $\gamma = 0.3$, $\gamma_2 = 13/3$, $b_2 = -3/710$ and $c_2 = 8/3$.

Schematic illustration of DIRK3 based scheme is represented in Fig. 1.

BDF methods

The backward differentiation formula (BDF) is a linear multi step method (see [38]), which gives uniformly accurate solution for all values of κ. The s order BDF method for $y' = g(t, y)$ is represented by

$$BDF: y^{n+1} = \sum_{k=1}^{s} \alpha_k y^{n+1-k} + \beta_s \Delta t g(t_{n+1}, y^{n+1}), \tag{36}$$

where α_k and β_s are constants depending on s. The main advantage of s order BDF method against a s-stage DIRK method is that it enables to design semi-Lagrangian schemes with fewer interpolations and computations of Maxwellian. Then, the BDF based SL scheme works as follows:

Algorithm for s-order BDF based methods

1. For $k = 1, \dots, s$, interpolate $f_{i,j}^{n,k} = f(x_i - k v_j \Delta t, v_j, t^{n+1-k})$ from $\left\{f_{i,j}^{n+1-k}\right\}_{i\in\mathcal{I}}$.
2. Compute:

$$f_{i,j}^{n+1} = \sum_{k=1}^{s} \alpha_k f_{i,j}^{n,k} + \beta_s \frac{\Delta t}{\kappa} \left(\mathcal{M}\left[f_i^{n+1}\right]_j - f_{i,j}^{n+1} \right),$$

where we compute the macroscopic moments of $\mathcal{M}\left[f_i^{n+1}\right]_j$ from $\left\{\sum_{k=1}^{s} \alpha_k f_{i,j}^{n,k}\right\}_{j\in\mathcal{J}}$.

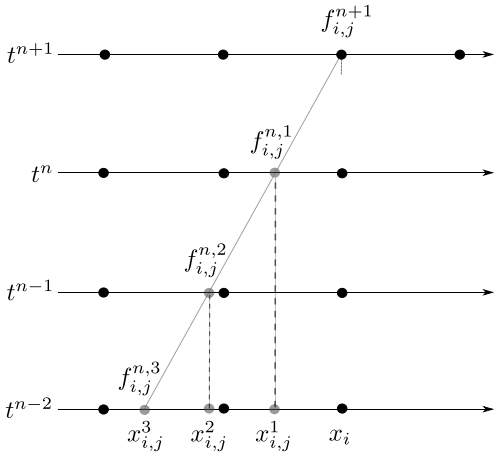

Fig. 2. Representation of BDF3 scheme. Black circles: grid nodes, grey circles: points where interpolation is needed.

For numerical tests, we will consider BDF3 ($s = 3$) method:

$$y^{n+1} = \frac{18}{11}y^n - \frac{9}{11}y^{n-1} + \frac{2}{11}y^{n-2} + \frac{6}{11}\Delta t g(y^{n+1}, t_{n+1}), \tag{37}$$

schematically illustrated in Fig. 2. We note that for each grid node in space and velocity, and for each time step, BDF3 scheme involves three interpolation and one evaluation of the Maxwellian, while DIRK3 based scheme performs six interpolations and three evaluations of the Maxwellian.

Remark 5.1. We remark that the positivity preserving property of semi-Lagrangian schemes for the BGK model is not straightforward even if we impose the positivity for spatial reconstructions. This is mainly due to the use of high order time discretizations such as DIRK and BDF methods. In particular, for DIRK methods, the values of $K_{i,j}^{(k,\ell)}$ can be negative. In case of BDF schemes, the negative values of α_k in (36) may lead to negative solutions. For these reasons, in this paper, we only impose conservation and non-oscillatory properties. (For a positive scheme to the BGK model in the Eulerian framework, we refer to [41].)

5.2.1. Asymptotic preserving property of SL schemes for the BGK model

In [14], we show that the first order scheme SL (21) with time discretization gives $f = \mathcal{M}(f) + \mathcal{O}(\kappa)$. The result can be easily extended to fully discretized high order SL schemes. Consider a general BDF scheme:

$$f_{i,j}^{n+1} = \frac{\kappa f_{i,j}^* + \beta_s \Delta t \mathcal{M}[f_i^*]_j}{\kappa + \beta_s \Delta t} \tag{38}$$

where $f_{i,j}^* = \sum_{k=1}^{s} \alpha_k f_{i,j}^{n,k}$ and $\mathcal{M}[f_i^*]_j$ is the Maxwellian constructed from $\{f_{i,j}^*\}_{j\in\mathcal{J}}$. Then, we can rewrite (38) as

$$\mathcal{M}[f_i^*]_j - f_{i,j}^{n+1} = \frac{\kappa}{\kappa + \beta_s \Delta t}\left(\mathcal{M}[f_i^*]_j - f_{i,j}^*\right) \tag{39}$$

Under the assumption that $f_{i,j}^*$, $\mathcal{M}[f_i^*]_j = \mathcal{O}(1)$ and $\beta_s \neq 0$, for a fixed time step $\Delta t >> \kappa$, we have

$$f_{i,j}^{n+1} = \mathcal{M}[f_i^*]_j + \mathcal{O}(\kappa) \tag{40}$$

for any $n \geq 0$ regardless of initial data. We furthermore note that the following identity holds: $\mathcal{M}[f_i^{n+1}]_j = \mathcal{M}[f_i^*]_j$ which comes from the fact that $\{f_{i,j}^{n+1}\}_{j\in\mathcal{J}}$ and $\{f_{i,j}^*\}_{j\in\mathcal{J}}$ have the same moments. Consequently, this together with (40) gives

$$f_{i,j}^{n+1} = \mathcal{M}[f_i^{n+1}]_j + \mathcal{O}(\kappa). \tag{41}$$

In a similar manner, DIRK based high order semi-Lagrangian methods also satisfy relation (41). In order to show that, we rewrite (34) in the following form

$$\mathcal{M}[F_i^{(k,k)}]_j - F_{i,j}^{(k,k)} = \frac{\kappa}{\kappa + a_{kk}\Delta t}\left(\mathcal{M}\left[\hat{F}_i^{(k,\ell)}\right]_j - \hat{F}_{i,j}^{(k,\ell)}\right),$$

where $\hat{F}_{i,j}^{(k,\ell)} = F_{i,j}^{(k,0)} + \Delta t \sum_{\ell=1}^{k-1} a_{k\ell} K_{i,j}^{(k,\ell)}$ and $\mathcal{M}\left[\hat{F}_i^{(k,\ell)}\right]_j$ is computed from $\left\{\hat{F}_{i,j}^{(k,\ell)}\right\}_{j\in\mathcal{J}}$. Recall that $\mathcal{M}\left[F_i^{(k,k)}\right]_j$ and $\mathcal{M}\left[\hat{F}_i^{(k,\ell)}\right]_j$ have the same moments. Then, this formally gives

$$\mathcal{M}[F_i^{(k,k)}]_j - F_{i,j}^{(k,k)} = \mathcal{O}(\kappa)$$

for the internal stages. Now, assuming that the DIRK scheme is SA, i.e., $f_{i,j}^{n+1} = F_{i,j}^{(s,s)}$, for the numerical solution we get

$$f_{i,j}^{n+1} = \mathcal{M}[f_i^{n+1}]_j + \mathcal{O}(\kappa).$$

Here we only showed that our solution converges to Maxwellian as $\kappa \to 0$. In order to show that our methods are *Asymptotic preserving* (AP), we present related numerical tests in Sect. 6.4.2 and 6.5.2. Note that another important property for a numerical scheme is the *Asymptotic Accuracy* (AA) property, i.e. the scheme is AP and in addition, it maintains its order of temporal accuracy when $\kappa \to 0$. Numerical tests in Sections 6.4.1 and 6.5.1 show that BDF schemes are AA, on the other hand, DIRK schemes are AP, but not AA. This means that such schemes exhibit a loss of accuracy in the limit $\kappa \to 0$. In the literature this is known as *order reduction phenomenon*. We conjecture that this order reduction appears because we can not avoid the influence of the interpolation in the internal stages that pollutes the temporal order. However, full understanding of the order reduction in this context deserves deeper analysis and it's beyond the scope of present paper.

6. Numerical tests

In this section, we test the performance of the proposed conservative high order semi-Lagrangian methods on the rigid body rotation (8), the Vlasov-Poisson system (1) and the BGK model (3).

For accuracy tests, we measure numerical errors and the corresponding convergence rate using a relative L^1-norm of the numerical solutions. For example, in case of 1D a space-time dependent solution $u(x,t)$, let $u_i^n(h)$ be the solution obtained by using $h = \Delta x$ with N_x grid points. Similarly, we denote by $u_i^n(h/2)$ the solution obtained with $h/2$ with $2N_x$ grid points.

- Relative L^1-norm of u^n using N_x

$$\text{error } (N_x, 2N_x) = \frac{\sum_{i=1}^{N_x^{dx}} |u_i^n(h) - u_{2i-1}^n(h/2)|}{\sum_{i=1}^{N_x^{dx}} |u_{2i-1}^n(h/2)|} \tag{42}$$

  We measure two-dimensional relative L^1-norm in the same way.
- Convergence rate

$$\text{Rate}(N_x) = \log_2\left(\frac{\text{error } (N_x, 2N_x)}{\text{error } (2N_x, 4N_x)}\right). \tag{43}$$

For two-dimensional problems, we assume uniform square meshes both in space and velocity domains, i.e., $\Delta x = \Delta y = h$ for space and $\Delta v^1 = \Delta v^2 = \Delta v$ for velocity. In two-dimensional accuracy tests, we will compute errors and convergence rates using relative L^1-norm as in (42) and (43).

6.1. Rigid body rotation

Since the analytical solution for rigid body rotation (8) preserves the shape, we designed high order conservative splitting methods to have both non-oscillatory and MPP properties.

For numerical tests, we take CWENO23, CWENO35 and CWENO47 reconstructions as basic reconstructions with a MPP limiter (6). (For details of CWENO, we refer to [21–24].) For comparison, as counterparts, we consider conservative polynomials of degree 3, 5 and 7 as basic reconstructions with a MPP limiter. Note that such polynomials of degree 3, 5 and 7 are the same optimal polynomials used for CWENO23, CWENO35 and CWENO47 reconstructions. The schemes compared in this test are reported in Table 2.

Here 2D-P3 is obtained by adopting, as a basic reconstruction, the two dimensional optimal polynomial of degree 2 used for 2D CWENO23 reconstruction [21]. Note that only 2D-P3-non-splitting does not use the MPP limiter.

We use the CFL number defined as

$$\text{CFL} = \Delta t\left(\frac{|y|_{max}}{\Delta x} + \frac{|x|_{max}}{\Delta y}\right). \tag{44}$$

In the following examples, the computational domain is the square $\Omega = [-\pi, \pi]^2$, therefore $|x|_{max} = |y|_{max} = \pi$.

Table 2
Numerical methods used for rigid body rotation.

Scheme	Order of time splitting method	Basic reconstruction
2-P3-MPP	2nd order Strang splitting (28)	P3
2-QCWENO23-MPP		CWENO23
4-P5-MPP	4th order Yoshida splitting (29)	P5
4-QCWENO23-MPP		CWENO23
4-QCWENO35-MPP		CWENO35
6-P7-MPP	6th order Yoshida splitting (30)	P7
6-QCWENO35-MPP		CWENO35
6-QCWENO47-MPP		CWENO47
2D-P3-non-splitting	Exact characteristics (Eq. (9))	2D-P3

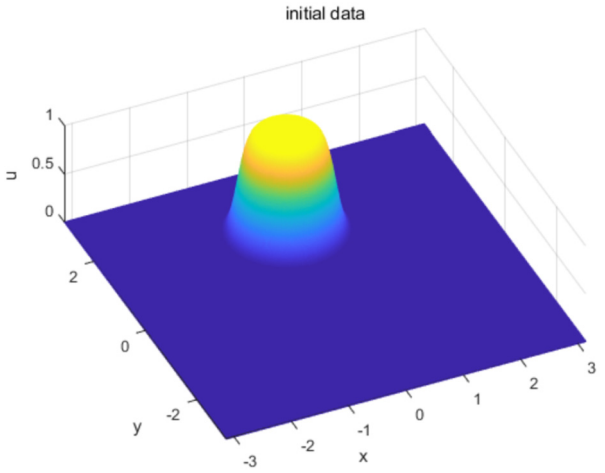

Fig. 3. Accuracy test for 2D Rigid body motion. Initial data given in (46).

6.1.1. Accuracy test

To confirm the accuracy of the proposed schemes, we consider the following smooth initial data

$$u_0(x, y) = f\left(\sqrt{x^2 + (y - 1.5)^2}\right), \quad x \in [-\pi, \pi], \quad y \in [-\pi, \pi], \tag{45}$$

where

$$f(r) = \begin{cases} 1, & r < \frac{1}{4} \\ p(r), & \frac{1}{4} \le r \le \frac{5}{4} \\ 0, & \text{otherwise} \end{cases}. \tag{46}$$

Here $p : \mathbb{R} \to \mathbb{R}$ is a polynomial of degree 16 determined by imposing 17 conditions, so that the piecewise polynomial function f is of class $C^7(\mathbb{R})$. In particular, we impose that the first 8 derivatives of $p(r)$ are continuous at $r = \frac{1}{4}$ and that the first 7 derivatives are continuous at $r = \frac{5}{4}$. We plot initial data in Fig. 3.

For space, we assumed zero-boundary condition, and compute numerical solutions at $t_f = 1$ with $N_x = N_y = 40, 80, 160, 320, 640$. We choose the time step imposing that the CFL number (44) has a prescribed value. To obtain fast convergence to the desired accuracy, in the CWENO basic reconstructions we adopt $\varepsilon = \Delta x$. (See [1], Eq. (18), and [24,42] for the choice of ε.)

In Table 3, we report the relative L^1-norm (42) and the corresponding convergence rates (43) of the numerical solution u. The results imply that the use of MPP limiter (6) does not introduce any order reduction. For CFL= 1.05, spatial errors are dominant, which gives the desired accuracy. On the other hand, for large CFL $= 8.4$, we observe the orders for time splitting methods which implies that time discretization errors are dominant. In Table 4, we also report L^1-conservation errors which correspond to results in Table 3. Here we see that L^1-norm is well preserved even for relatively coarse grid $N_x = 80$. Finally, we perform a comparison among the schemes in terms of error versus cpu time. The result is shown in Fig. 4. It appears that second order method is more efficient for lower accuracy while sixth order method is more efficient if higher accuracy is required. As a remark, we additionally present numerical results obtained by the non-splitting semi-Lagrangian method for rigid body rotation which makes use of exact characteristics. Here the only error (besides round off) is due to interpolation. In Table 5, we report numerical errors obtained with different time steps: (1) Δt is determined by

Table 3
Accuracy test for splitting methods of rigid body rotation with initial data (46).

Scheme	$(N_x, 2N_x)$	CFL = 1.05		CFL = 8.4	
		Error	Rate	Error	Rate
	(40, 80)	4.3025e-02	2.12	2.4377e-01	1.98
2-QCWENO23	(80, 160)	9.8567e-03	2.30	6.1939e-02	1.92
MPP	(160, 320)	2.0039e-03	2.97	1.6316e-02	1.98
	(320, 640)	2.5531e-04		4.1422e-03	
	(40, 80)	7.0672e-02	1.95	1.3951e-01	3.83
4-QCWENO23	(80, 160)	1.8288e-02	2.06	9.8361e-03	3.40
MPP	(160, 320)	4.3970e-03	2.83	9.3254e-04	3.19
	(320, 640)	6.1634e-04		1.0186e-04	
	(40, 80)	4.2412e-02	2.92	1.4000e-01	4.26
4-QCWENO35	(80, 160)	5.5900e-03	4.06	7.3184e-03	4.06
MPP	(160, 320)	3.3613e-04	4.94	4.3762e-04	3.97
	(320, 640)	1.0976e-05		2.7920e-05	
	(40, 80)	6.6372e-02	2.89	3.1024e-01	6.22
6-QCWENO35	(80, 160)	8.9840e-03	3.40	4.1687e-03	4.78
MPP	(160, 320)	8.4956e-04	4.89	1.5141e-04	5.03
	(320, 640)	2.8626e-05		4.6439e-06	
	(40, 80)	2.3053e-02	3.08	3.0354e-01	8.10
6-QCWENO47	(80, 160)	2.7278e-03	5.31	1.1058e-03	5.74
MPP	(160, 320)	6.8834e-05	6.92	2.0731e-05	6.17
	(320, 640)	5.6901e-07		2.8779e-07	

Table 4
Conservation errors obtained by splitting methods for rigid body rotation with initial data (46).

Scheme	N_x	CFL = 1.05	CFL = 8.4
		L^1 error	L^1 error
	80	0.0000e-00	3.5927e-16
2-QCWENO23	160	3.5927e-16	1.7964e-16
MPP	320	1.7964e-16	7.1854e-16
	640	3.5927e-16	5.3891e-16
	80	1.7964e-16	0
4-QCWENO23	160	3.5927e-16	3.5927e-16
MPP	320	1.7964e-16	8.9818e-16
	640	1.7964e-16	1.7964e-16
	80	1.9034e-12	1.6167e-15
4-QCWENO35	160	2.6406e-14	3.0538e-15
MPP	320	5.2992e-14	7.1854e-15
	640	1.0706e-13	1.3473e-14
	80	1.9040e-10	4.5794e-12
6-QCWENO35	160	7.3291e-14	9.5207e-15
MPP	320	1.4586e-13	1.8323e-14
	640	2.8921e-13	3.7185e-14
	80	1.4654e-11	1.1856e-14
6-QCWENO47	160	1.7964e-16	7.1854e-16
MPP	320	1.4371e-15	8.9818e-16
	640	3.5927e-15	0.0000e-00

CFL= 1.05, 8.4 in (44) (2) $\Delta t = t_f = 1$. For CFL = 1.05, 8.4, the global accuracy is degraded by one as expected, hence it is close to 3. On the other hand, one-step based method ($\Delta t = 1$ case) does not have an order reduction, so it gives order 4 which is the accuracy of QCWENO23 reconstruction for smooth functions. In Table 6, we report L^1-conservation errors which correspond to results in Table 5. Compared to results in Table 4, sufficient large number of grid points should be secured to preserve L^1-norm in the non-splitting based method.

6.1.2. Maximum principle preserving and non-oscillatory properties

In this example, we show that the combined use of CWENO reconstructions and MPP limiter for the basic reconstruction enables to achieve both non-oscillatory property and maximum principle preserving property at the same time.

For this, we consider initial data composed of a slotted disk, a cone and a smooth hump, as in [43], together with a double layered disk. We plot initial data in Fig. 5 and compute numerical solutions with CFL = 6.3. In Fig. 6, we compare numerical methods listed in Table 2. In particular, we plot contours and slides of numerical solutions at different locations

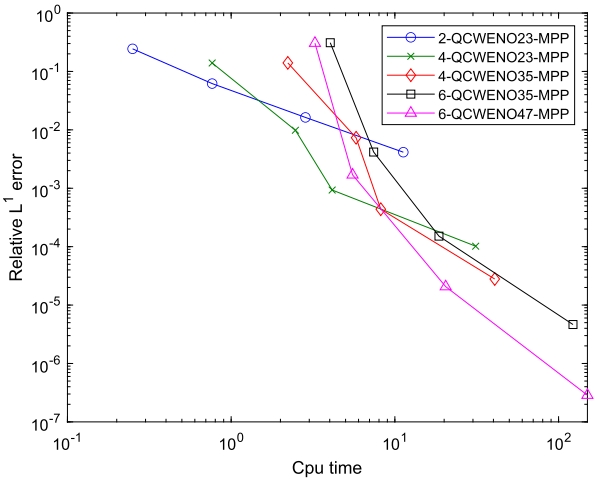

Fig. 4. 2D Rigid body motion. Error versus cpu time.

Table 5
Accuracy test for 2D-P3-non-splitting method of rigid body rotation with initial data (46).

Scheme	$(N_x, 2N_x)$	CFL $= 1.05$		CFL $= 8.4$		$\Delta t = t_f = 1$	
		Error	Rate	Error	Rate	Error	Rate
	(40, 80)	4.4767e-02	2.1738	1.5350e-02	2.9408	8.7760e-03	3.5933
2D-P3	(80, 160)	9.9211e-03	2.7599	1.9991e-03	3.2646	7.2713e-04	3.9797
non-splitting	(160, 320)	1.4647e-03	2.9500	2.0802e-04	2.9769	4.6088e-05	3.9874
	(320, 640)	1.8955e-04		2.6423e-05		2.9058e-06	

Table 6
Conservation errors in mass obtained by 2D-P3-non-splitting for rigid body rotation with initial data (46).

Scheme	N_x	Mass error		
		CFL $= 1.05$	CFL $= 8.4$	$\Delta t = 1$
	80	9.9358e-07	2.7724e-06	5.7758e-07
2D-P3	160	2.5417e-08	1.2029e-07	9.5474e-10
non-splitting	320	5.8763e-11	8.3774e-10	8.1131e-11
	640	5.6213e-12	4.9656e-11	2.3963e-13

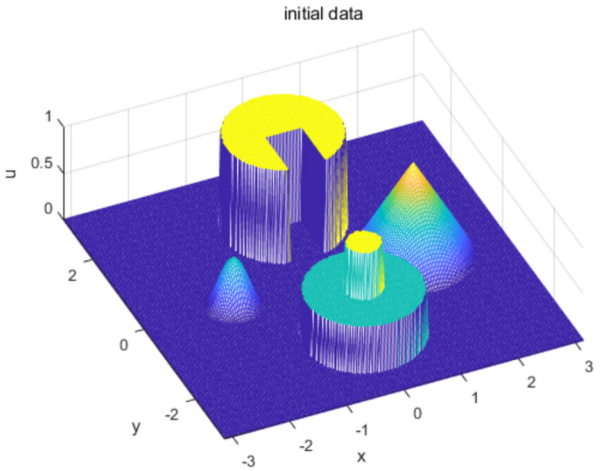

Fig. 5. 2D Rigid body motion. Initial data used for results in Fig. 6.

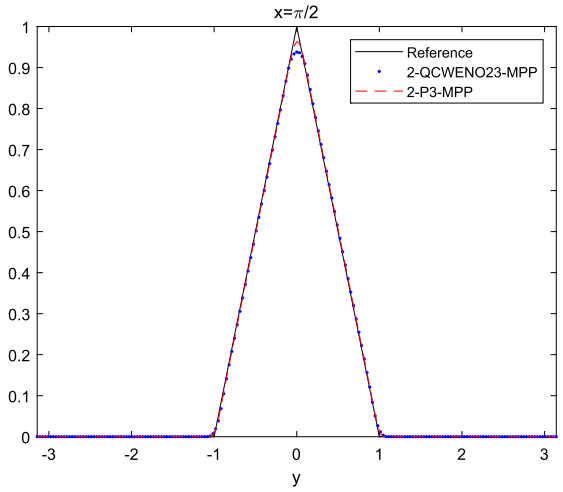

(a) Cone

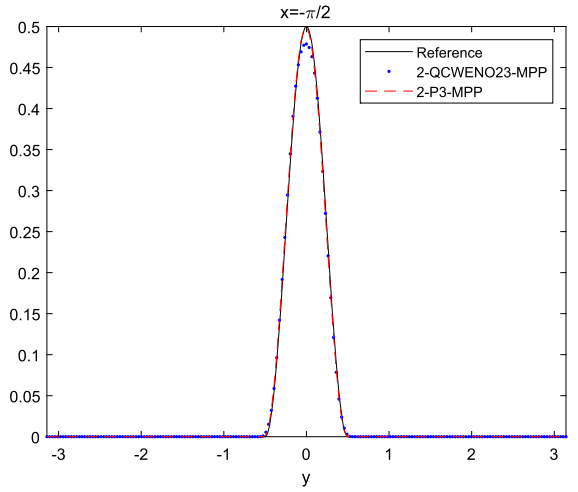

(b) Hump

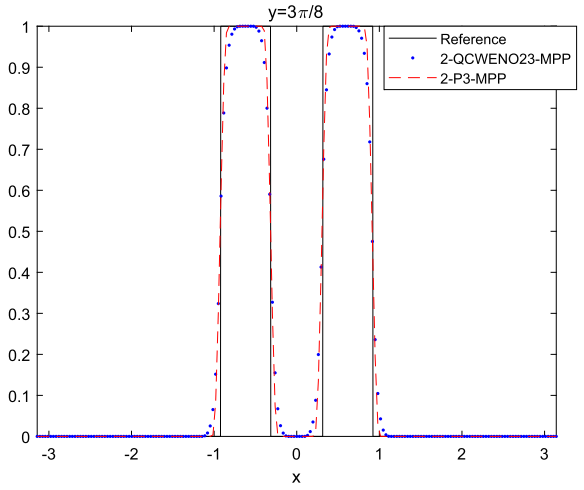

(c) Cylinder

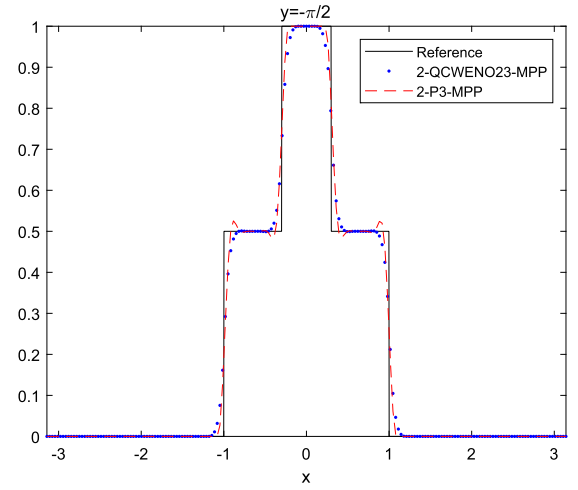

(d) Double layer

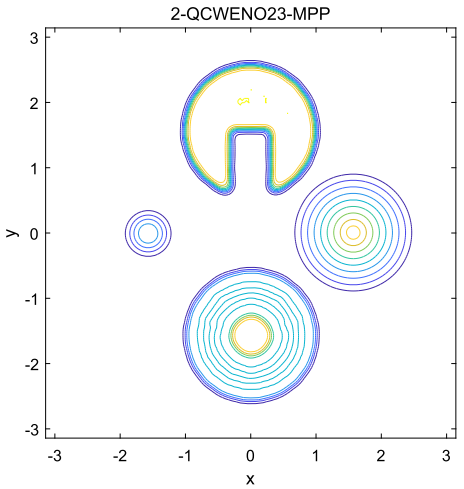

(e) Contour

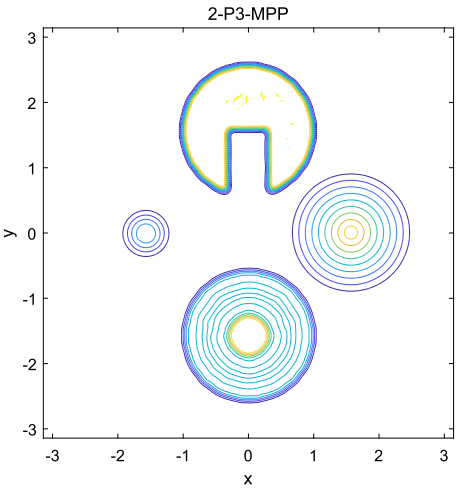

(f) Contour

Fig. 6. 2D Rigid body motion. Numerical solutions obtained for $(N_x, N_y) = 192 \times 192$. For CWENO23, we use $\varepsilon = 10^{-4}$.

Table 7
Numerical methods with MPP limiter used for the 1D Vlasov-Poisson model.

Scheme	Order of time splitting method	Basic reconstruction
2-P3-MPP	2nd order Strang splitting method (28)	P3
4-P5-MPP	4th order Yoshida splitting (29)	P5
6-P7-MPP	6th order method in (33)	P7

at final time $t_f = 2\pi$. In Figs. 6a and 6b, the use of non-linear weights makes CWENO based methods more dissipative than MPP-based schemes. Although such dissipative tendency can be improved using high order CWENO based methods, these non oscillatory reconstructions do not seem to be necessary for the numerical treatment of cone and hump. We also note that there is no negative solution due to the use of MPP limiter. In Fig. 6c, examples for cylinder show more evident effects of the MPP limiter near the maximum ($u = 1$) and the minimum ($u = 0$). In panel 6d of the same figures one can see that the MPP limiter is not enough to prevent oscillations in the middle layer. When using CWENO35 or CWENO47 in place of CWENO23 as basic reconstruction, we obtain similar results which we omit to report, with a slightly sharper resolution near singularities. These results verify that combining QCWENO with MPP limiter provides a high order conservative reconstruction which avoids spurious oscillation and maintains the maximum principle preserving property at the same time.

We remark that a careful choice of ε in CWENO is necessary to properly balance resolution and non-oscillatory property of the reconstruction. If ε is too large, non-linear weights reduce to linear weights, which do not prevent oscillations, while if ε is too small, the resulting reconstruction becomes too dissipative. In this numerical test, we simply set $\varepsilon = 10^{-4}$ for all CWENO reconstructions. For the optimal choice of ε and non-linear weights for CWENO reconstruction, we refer to [24,42,44].

6.2. 1D Vlasov-Poisson model

In this section we apply the high order splitting schemes described in Section 5.1 to the Vlasov-Poisson system.

To maintain conservation and MPP properties of analytical solutions for (1), we consider the numerical methods in Table 7.

For 1D problems $(d_x, d_v) = (1, 1)$, we adopted a uniform mesh Δx and Δv both in space and velocity. The CFL number is defined as

$$\mathrm{CFL} := \max\left\{\max_j |v_j|\frac{\Delta t}{\Delta x}, \max_i |\mathbb{E}_i|\frac{\Delta t}{\Delta v}\right\}. \tag{47}$$

6.2.1. Accuracy test

The aim of this section is to check the accuracy of high order splitting methods for the Vlasov-Poisson system. Here, we consider the following smooth initial data [45]:

$$f(x, v, 0) = \frac{2}{7\sqrt{2\pi}}(1 + 5v^2)\left(1 + \alpha\big((\cos(2kx) + \cos(3kx))/1.2 + \cos(kx)\big)\right)\exp\left(-\frac{v^2}{2}\right), \quad \alpha = 0.01, \quad k = 0.5. \tag{48}$$

We assume periodic boundary condition on the interval $[0, 4\pi]$ and zero-boundary condition on velocity domain $[-8, 8]$. Using (47), we take a time step determined by (47) with CFL $= 6, 30, 80$.

From Table 7, we note that each numerical scheme takes a spatial reconstruction whose order is higher than that of time splitting method. This means that for a fixed CFL number and sufficiently refined grid in all independent variables, spatial errors become smaller than time errors, especially for large CFL numbers and/or long integration time. On the contrary, we can expect that convergence rates for reconstructions are easily confirmed for a small CFL numbers and/or short integration time.

For these reasons, we consider three cases for accuracy tests: (1) $N_x = N_v = 40, 80, 160, 320, 640$ with CFL $= 6$, (2) $N_x = N_v = 80, 160, 320, 640, 1280$ with CFL $= 30$, (3) $N_x = N_v = 160, 320, 640, 1280, 2560$ with CFL $= 80$. Here we check the accuracy of all schemes based on the relative L^1-errors (42) and convergence rates (43) of the numerical solutions f at a final time $t_f = 2$.

The final time is relatively short: a typical particle will move only a fraction of the domain before time t_f. In Table 8, we report numerical results for all schemes. As expected, for CFL $= 80$ we obtain the convergence rates of time splitting methods. On the contrary, for relatively small CFL $= 6$ we observe the accuracy of spatial reconstructions. In both cases, we note that the use of MPP limiter does not lead to any order reduction. In case of CFL $= 30$, we observe intermediate results between the two extreme cases. Similarly to the case of rotation problem, the efficiency of schemes applied to the Vlasov-Poisson system is compared and the results are shown in Fig. 7.

6.2.2. 1D Long time simulation

Next, we move on to long time simulations for VP system.

Table 8
Accuracy test for the 1D Vlasov-Poisson system. Initial data is given in (48).

	$(N_x, 2N_x)$	2-P3-MPP		4-P5-MPP		6-P7-MPP	
		Error	Rate	Error	Rate	Error	Rate
	(40, 80)	9.6342e-04	2.8326	9.2861e-04	4.6418	6.3265e-05	6.5140
CFL = 6	(80, 160)	1.3524e-04	2.8548	3.7198e-05	4.8619	6.9221e-07	6.8646
	(160, 320)	1.8695e-05	2.7401	1.2792e-06	4.8827	5.9401e-09	6.9705
	(320, 640)	2.7981e-06		4.3361e-08		4.7365e-11	
	(80, 160)	7.9790e-04	2.4358	1.0121e-03	3.4034	7.0842e-07	6.9204
CFL = 30	(160, 320)	1.4747e-04	2.0432	9.5658e-05	3.7276	5.8487e-09	6.9745
	(320, 640)	3.5779e-05	1.8966	7.2211e-06	3.8933	4.6506e-11	6.9745
	(640, 1280)	9.6092e-06		4.8595e-07		3.6982e-13	
	(160, 320)	1.5142e-03	2.4288	1.9771e-03	2.7746	7.0569e-07	8.7136
CFL = 80	(320, 640)	2.8122e-04	2.0837	2.8893e-04	3.6838	1.6810e-09	5.9542
	(640, 1280)	6.6341e-05	2.0194	2.2483e-05	3.9038	2.7113e-11	5.9407
	(1280, 2560)	1.6364e-05		1.5020e-06		4.4141e-13	

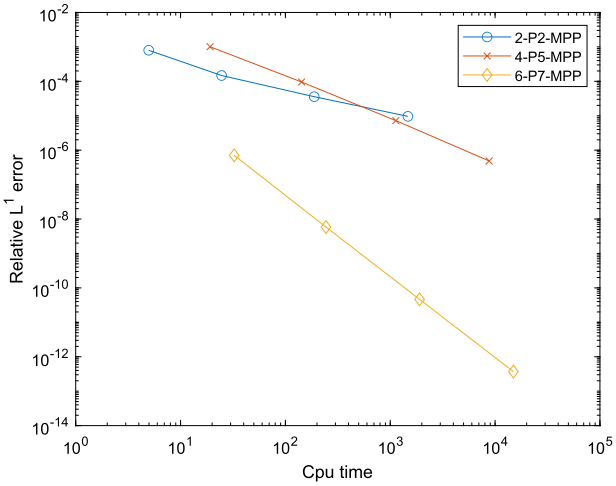

Fig. 7. 1D Vlasov Poisson. Error versus cpu time. (For interpretation of the references to colour in this figure, the reader is referred to the web version of this article.)

The Vlasov-Poisson system admits several time invariants, such as L^p-norms of the solution total energy and entropy. These quantities can be used as diagnostics for the numerical methods. Here we monitor, the following four quantities that should remain constant in time:

- L^p-norm of f^n, $p = 1, 2$

$$\|f^n\|_p = \left(\sum_{i,j} |f^n_{i,j}|^p (\Delta x)^{d_x} (\Delta v)^{d_v} \right)^{1/p}.$$

- Total energy of f^n

$$\text{Energy} = \sum_{i,j} \frac{|v_j|^2}{2} f^n_{i,j} (\Delta x)^{d_x} (\Delta v)^{d_v} + \sum_i \frac{|\mathbb{E}^n_i|^2}{2} (\Delta x)^{d_x}.$$

- Entropy of f^n

$$\text{Entropy} = -\sum_{i,j} f^n_{i,j} \log f^n_{i,j} (\Delta x)^{d_x} (\Delta v)^{d_v}.$$

In addition, we monitor the behaviour of the electric field:

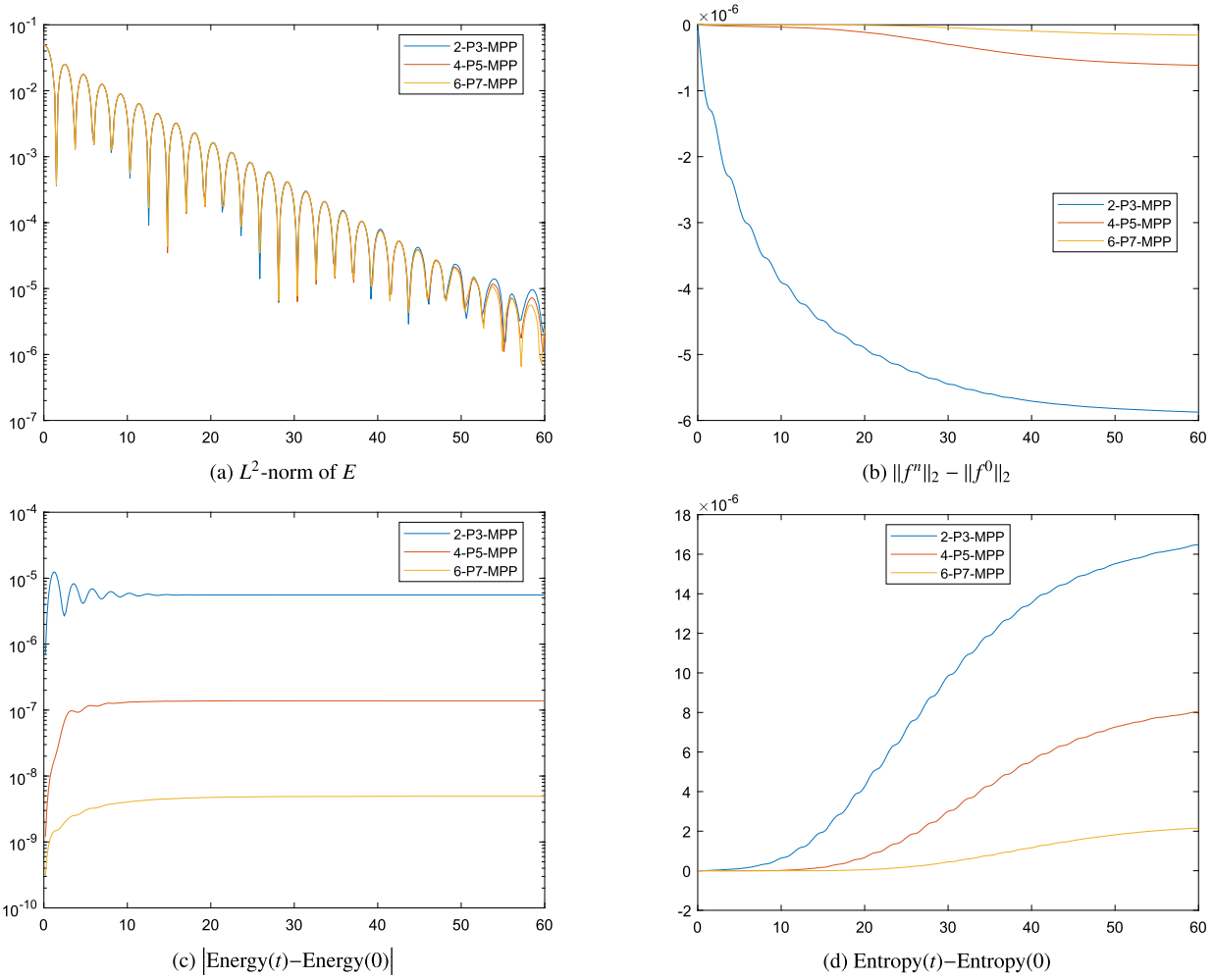

Fig. 8. Weak Landau damping in the 1D Vlasov Poisson. $N_x = 64$, $N_v = 128$.

Table 9
Weak Landau damping in the 1D Vlasov Poisson. $|\,\|f^{N_t}\|_1 - \|f^0\|_1\,|$.

	(N_x, N_v)	2-P3-MPP	4-P5-MPP	6-P7-MPP
		Error	Error	Error
$\max_j \|v_j\| = 2\pi$	(64, 128)	2.7274e-10	4.1143e-10	2.4873e-10
$\max_j \|v_j\| = 2.5\pi$	(64, 160)	7.1054e-15	3.6344e-12	1.9540e-14

- L^2-norm of $\mathbb{E}^n$

$$\|\mathbb{E}^n\|_2 = \left(\sum_i |\mathbb{E}_i^n|^2 (\Delta x)^{d_x}\right)^{1/2}.$$

We consider two benchmark problems in [46] with the following initial data:

$$f(x, v, 0) = \frac{1}{\sqrt{2\pi}}\left(1 + \alpha\cos(kx)\right)\exp\left(-\frac{v^2}{2}\right), \tag{49}$$

where we use $(\alpha, k) = (0.01, 0.5)$ for weak Landau damping, and $(\alpha, k) = (0.5, 0.5)$ for strong Landau damping.

For both problems, we impose periodic boundary condition on the physical domain $[-2\pi, 2\pi]$ and zero-boundary condition on velocity domain $[-2\pi, 2\pi]$. Numerical solutions are computed up to final time $t_f = 60$ with a time step determined by CFL $= 6$ using (47). The grid size is $N_x = 64$ and $N_v = 128$.

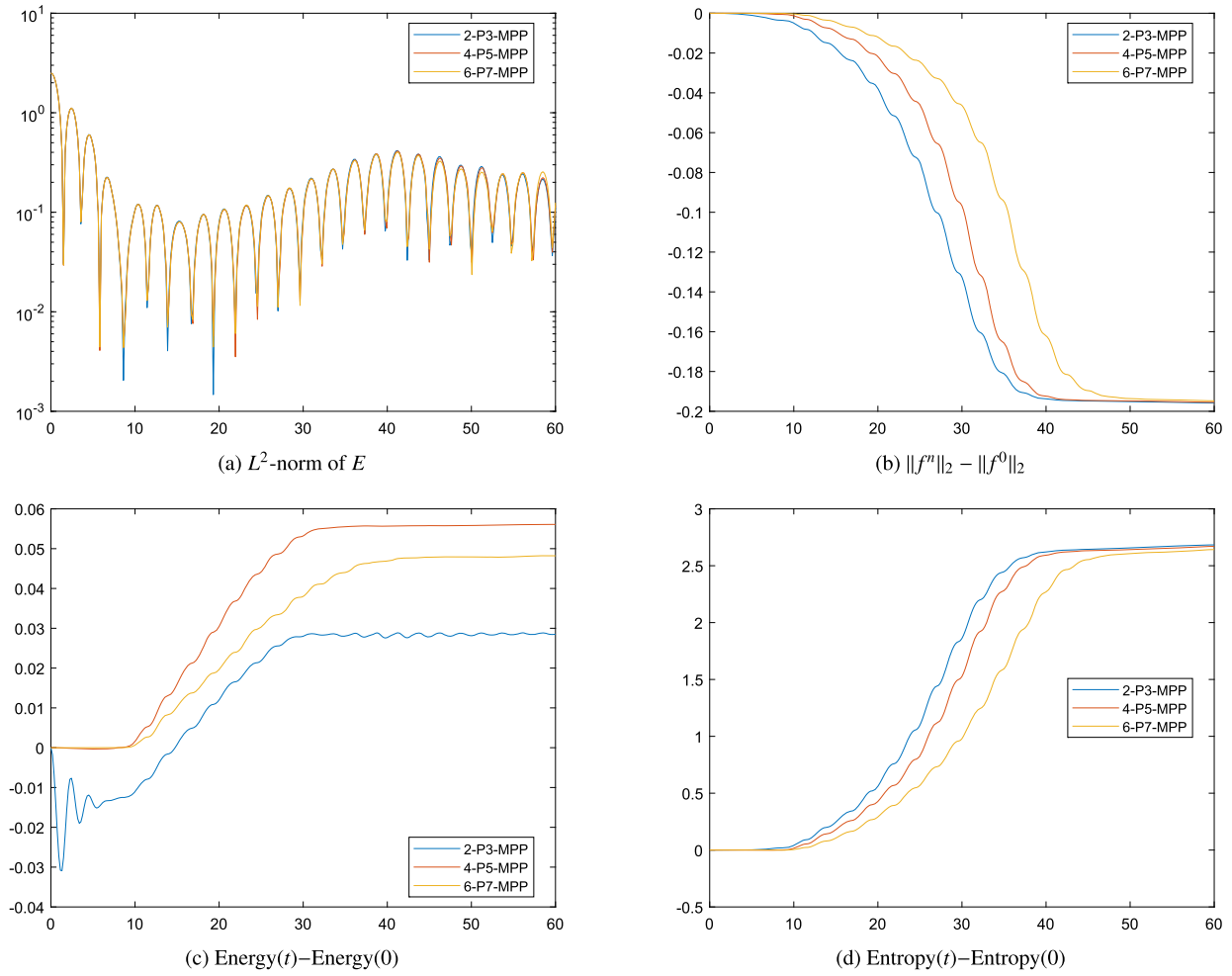

(a) L^2-norm of E (b) $\|f^n\|_2 - \|f^0\|_2$

(c) Energy(t)−Energy(0) (d) Entropy(t)−Entropy(0)

Fig. 9. Strong Landau damping in the 1D Vlasov Poisson. $N_x = 64$, $N_v = 128$.

Table 10
Strong Landau damping in the 1D Vlasov Poisson. $\left| \|f^{N_t}\|_1 - \|f^0\|_1 \right|$.

	(N_x, N_v)	2-P3-MPP	4-P5-MPP	6-P7-MPP
		Error	Error	Error
$\max_j \|v_j\| = 2\pi$	(64, 128)	4.3616e-08	6.5483e-08	5.0082e-08
$\max_j \|v_j\| = 2.5\pi$	(64, 160)	4.6185e-13	2.5722e-12	6.9633e-13

In Fig. 8, we plot numerical results obtained by high-order splitting methods listed in Table 7. The time evolution of L^2-norm of the electric field $\mathbb{E}^n$ shows a theoretical damping rate for all schemes. After $t = 50$, only scheme 6-P7-MPP maintains the correct damping rate.

Regarding the preservation of conserved quantities such as the L^2-norm/energy/entropy of numerical solutions, all schemes produce small conservation errors within 10^{-6}. Among them, the 6-P7-MPP scheme gives the most accurate profiles. These results are comparable with those obtained with other conservative finite difference methods available in the literature, such as, for example, [47].

In Table 9, we also report the L^1-norm of f at final time for two different velocity domains. When we increase the size of the domain by 25% keeping Δv unchanged, the error decreases by orders of magnitude, confirming that the lack of conservation is only due to finite computational domain.

For strong Landau damping, we first compute numerical solutions taking the same domain and meshes used for the weak Landau damping. In Fig. 9, numerical results are plotted for $N_x = 64$, $N_v = 128$ with velocity domain $[-2\pi, 2\pi]$. Due to the increased perturbation amplitude $\alpha = 0.5$, non-linear damping begins to appear around $t = 10$. Such non-linear tendency of the electric field is well-captured by each scheme, but all conservation errors are non negligible.

In Table 10, the small error in the L^1-norm is due to the loss of conservation caused by zero-boundary condition at the edge of the computational domain in velocity. If we slightly enlarge the domain in velocity space, say from $[-2\pi, -2\pi]$ to

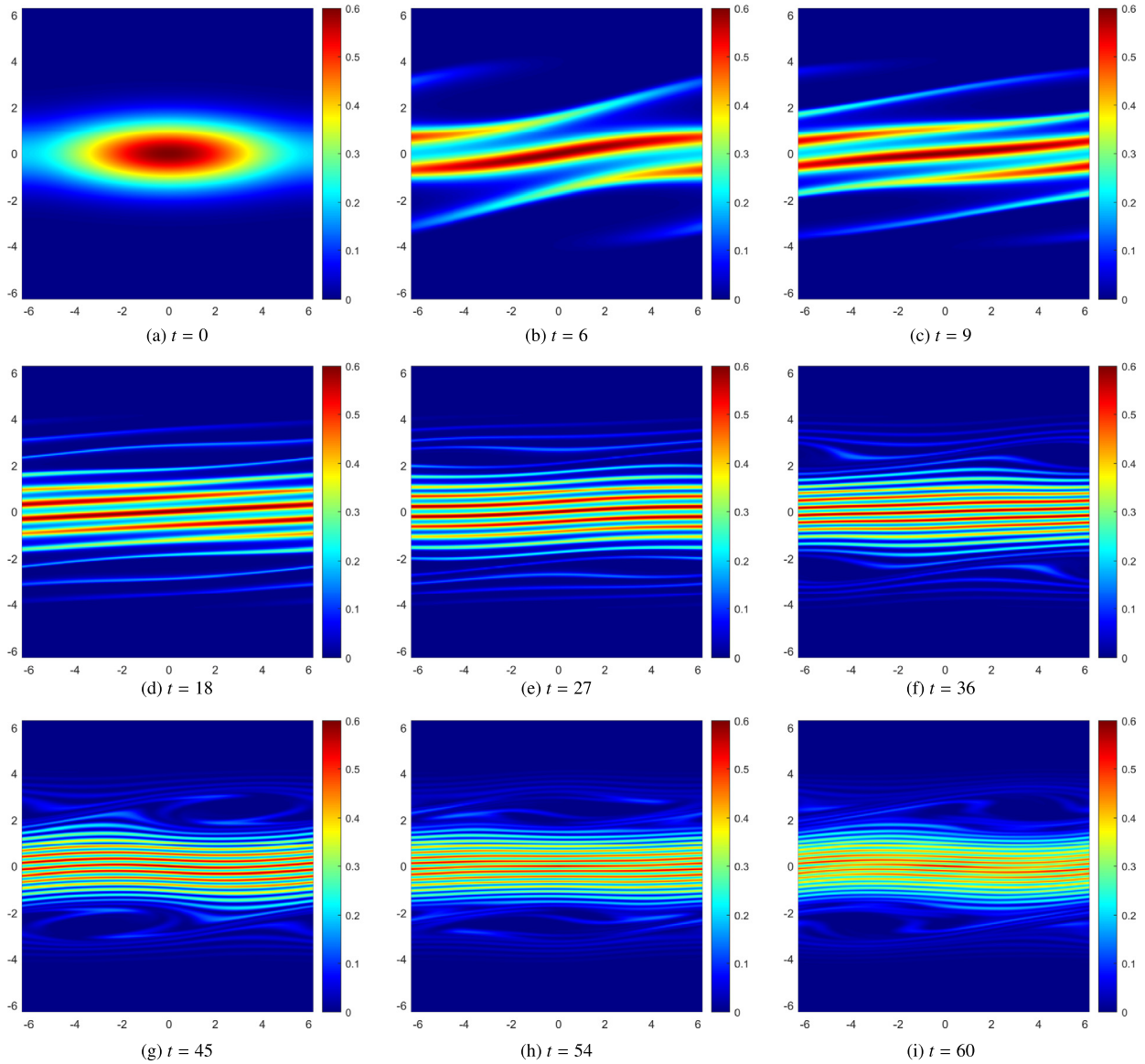

Fig. 10. Phase space portrait of the distribution function in the case of strong Landau damping in the 1D Vlasov Poisson. Here we use a velocity domain $[-2\pi, 2\pi]$ with $N_x = 128$, $N_v = 256$.

$[-2.5\pi, -2.5\pi]$, then conservation of L^1 norm improves by four orders of magnitude. Although all schemes exhibit finite conservation errors in L^2-norm, entropy and energy, we confirm that scheme 6-P7-MPP has less conservation errors than schemes 2-P3-MPP and 4-P5-MPP. For comparison with the results in [46], we plot the distribution functions in phase space at different times in Fig. 10.

6.3. 2D Vlasov-Poisson model

In 2D problem $(d_x, d_v) = (2, 2)$, we take uniform mesh $\Delta x = \Delta y$ for space and Δv for each velocity dimension. We use a CFL number defined by

$$\text{CFL} := \max\left\{ \max_j |v_j^1| \frac{\Delta t}{\Delta x} + \max_j |v_j^2| \frac{\Delta t}{\Delta y},\ \max_i |E_i^1| \frac{\Delta t}{\Delta v} + \max_i |E_i^2| \frac{\Delta t}{\Delta v} \right\}, \tag{50}$$

for $E_i \equiv (E_i^1, E_i^2)$.

Table 11
Accuracy test for the 2D Vlasov-Poisson system. Initial data is given in (51).

$(N_x^2, (2N_x)^2)$	CFL = 1		CFL = 2		CFL = 3		CFL = 4		CFL = 5	
	Error	Rate	Error	Rate	Error	Rate	Error	Rate	Error	Rate
$(20^2, 40^2)$	1.19e-03	2.8278	1.24e-03	2.73	1.43e-03	2.46	2.22e-03	2.47	2.55e-03	2.11
$(40^2, 80^2)$	1.68e-04		1.87e-04		2.61e-04		4.01e-04		5.92e-04	

6.3.1. Accuracy test

To check the accuracy of splitting methods for the 2D Vlasov-Poisson system, we consider a setup in [17], where the initial data is given by

$$f(x, y, v^1, v^2, 0) = \frac{1}{2\pi}\left(1 + \alpha\big(\cos(kx) + \cos(ky)\big)\right)\exp\left(-\frac{|v^1|^2 + |v^2|^2}{2}\right), \quad \alpha = 0.05, \quad k = 0.5. \tag{51}$$

We impose periodic boundary condition on the space domain $[0, 4\pi]^2$ and assume zero-boundary condition on velocity domain $[-6, 6]^2$. Numerical solutions are computed up to final time $t_f = 2$ taking uniform grids with $N_x = N_y = N_{v_1} = N_{v_2} = 20, 40, 80$ and different time steps based on CFL $= 1, 2, 3, 4, 5$ using (50).

In this test, we consider a semi-Lagrangian method based on 2nd order Strang splitting method, i.e. in the advection step we solve (31) and in the drift step we solve (32). Note that we can solve each step without dimensional splitting, because during the advection step the velocities are constant in time, and during the drift step the electric field is constant in time. For a basic reconstruction, together with MPP limiter, we again take 2D-P3, which is the two-dimensional optimal polynomial of degree 2 used for CWENO23 reconstruction [21].

In Table 11, we report errors based on relative L^1-norm (42) and convergence rates (43) for two-dimensional solutions ($d_x = d_v = 2$). The results show that, for smaller CFL numbers, numerical errors tend to be smaller, and the desired accuracy of spatial reconstruction appears. On the contrary, as CFL number gets bigger, the expected accuracy of a time splitting method is observed. As in 1D case, the use MPP limiter does not lead to order reduction.

6.3.2. 2D Long time simulations

For the 2D Vlasov-Poisson model, we again consider a strong Landau damping problem as in [48]:

$$f(x, y, v^1, v^2, 0) = \frac{1}{2\pi}\left(1 + \alpha\big(\cos(kx) + \cos(ky)\big)\right)\exp\left(-\frac{|v^1|^2 + |v^2|^2}{2}\right), \quad \alpha = 0.5, \quad k = 0.5. \tag{52}$$

We impose periodic boundary condition in space domain $[0, 4\pi]^2$ and zero-boundary condition in velocity domain $[-6, 6]^2$. Using the scheme based on Strang splitting and 2D-P3, numerical solutions are computed up to final time $t_f = 40$. Here take a fixed time step $\Delta t = \frac{1}{8}$, and we set $N_x = N_y = 32$ and $N_{v^1} = N_{v^2} = 128$.

As in 1D case, Fig. 11 shows that a phase transition appears for the L^2-norm of electric field during time evolution, in agreement with what already obtained in [48]. At final time, due to the truncation of velocity domain, the L^1-norm of the numerical solution is maintained with a loss equal to 6.67×10^{-6}, which is reduced to 2.02×10^{-10} by using the 25% enlarged velocity domain $[-7.5, 7.5]^2$ and same Δv. The other conservative quantities such as L^2-norm, entropy, energy are not fully conserved at a numerical level.

6.4. 1D BGK model

Now, we move on to the numerical tests of SL schemes for the BGK model. After checking the accuracy of non-splitting semi-Lagrangian methods, we treat a related shock problem arising in the fluid limit $\kappa \to 0$. In 1D problem $(d_x, d_v) = (1, 1)$, we again consider uniform mesh Δx and Δv for space and velocity domain. For the 1D BGK model, we use a CFL number defined by

$$\text{CFL} := \max_j |v_j| \frac{\Delta t}{\Delta x}. \tag{53}$$

6.4.1. Accuracy test

To check accuracy, we consider a test proposed in [49]. The initial distribution is given by the Maxwellian

$$f_0(x, v) = \frac{\rho_0}{\sqrt{2\pi T_0}} \exp\left(-\frac{|v - u_0(x)|^2}{2T_0}\right), \tag{54}$$

where initial density and temperature are assumed to be uniform, with constant value $\rho_0(x) \equiv 1$ and $T_0(x) \equiv 1$. Initial velocity profile is given by

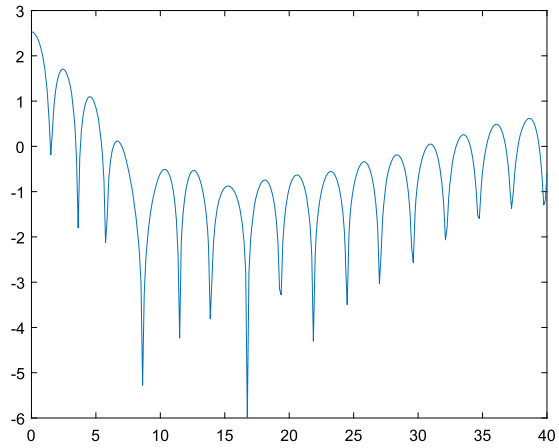

(a) Logarithmic scale of L^2-norm of E

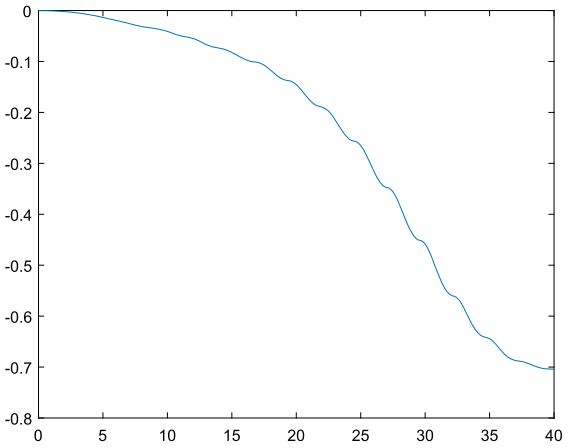

(b) $\|f^{N_t}\|_2 - \|f^0\|_2$

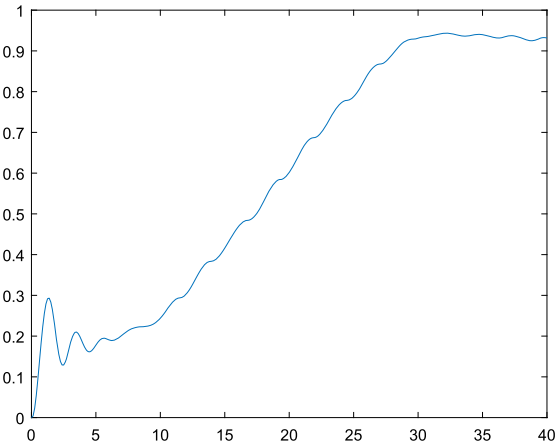

(c) Energy(t)−Energy(0)

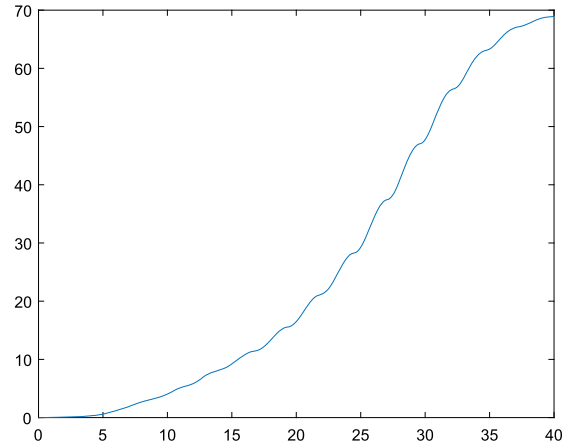

(d) Entropy(t)−Entropy(0)

Fig. 11. 2D Vlasov Poisson. Strong Landau damping with initial data (52). $N_x = N_y = 32$, $N_v^1 = N_v^2 = 128$.

$$u_0(x) = 0.1 \exp\left(-(10x-1)^2\right) - 2\exp\left(-(10x+3)^2\right).$$

For space, we assume periodic boundary conditions in the interval $[-1, 1]$ with $N_x = 320$, 640, 1280, 2560 and 5120. For velocity domain, we consider the interval $[-10, 10]$ with $N_v = 20$, which is enough when we use correction (23), as described in Section 4.3.2. We set time steps using (53) with CFL $= 4$, and compute numerical solutions up to $t_f = 0.32$ because for small Knudsen number shock appears at $t = 0.35$. For RK3 and BDF3 based methods, denoted respectively by RK3-QCWENO23 and BDF3-QCWENO23, we use QCWENO23 reconstruction, and hence we expected a convergence rate of approximately 3. In Table 12, we report errors and convergence rate computed with the relative L^1-norm for density ρ, as in (42) and (43). The result shows that order reductions appear for RK3 based method as $\kappa \to 0$, while it attains the expected order 3 of reconstruction for $\kappa = 1$. On the contrary, BDF3 does not suffer from order reduction and gives the desired convergence rate 3 for all values of κ. We remark that similar results are obtained for other macroscopic quantities such as momentum and energy, but we omit to show them here.

Since semi-Lagrangian schemes allow large CFL numbers, the choice of CFL number is important to secure both accuracy and efficiency. For such a reason we compute the errors obtained with different values of CFL numbers for various Knudsen numbers. In Fig. 12, we report the relative L^1 errors obtained by $N_x = 160,\ 320$ for each scheme. From Fig. 12, we observe that the error has a non monotone behaviour with respect to the CFL number. This is due to the fact that for smaller time steps Δt the interpolation error accumulates more frequently, making it dominant for small enough CFL numbers; the behaviour is in agreement with consistency analysis of semi-lagrangian schemes, as illustrated, for example in the book by Falcone and Ferretti [50], chapter 6. As a consequence there is an optimal CFL number that depends on the Knudsen number, and is in general larger than one. For large enough Courant number the error increases with CFL, as expected. Similar results are obtained using a different DIRK3 scheme, such as the one adopted in [5].

Table 12
Accuracy test for the 1D BGK equation. Initial data is given in (54). Here we used CFL = 4.

Relative L^1 error and order of density									
Scheme	$(N_x, 2N_x)$	$\kappa = 10^{-6}$		$\kappa = 10^{-4}$		$\kappa = 10^{-2}$		$\kappa = 10^{-0}$	
		Error	Rate	Error	Rate	Error	Rate	Error	Rate
RK3-QCWENO23	(320, 640)	2.56e-05	2.30	2.24e-05	2.47	2.10e-06	2.90	1.51e-05	3.94
	(640, 1280)	5.19e-06	2.08	4.05e-06	2.27	2.82e-07	2.87	9.83e-07	3.44
	(1280, 2560)	1.23e-06		8.42e-07		3.86e-08		9.09e-08	
BDF3-QCWENO23	(320, 640)	2.79e-05	2.97	2.50e-05	3.00	1.38e-06	3.16	1.07e-05	2.99
	(640, 1280)	3.56e-06	3.04	3.12e-06	3.04	1.54e-07	3.08	1.34e-06	3.00
	(1280, 2560)	4.34e-07		3.80e-07		1.83e-08		1.69e-07	

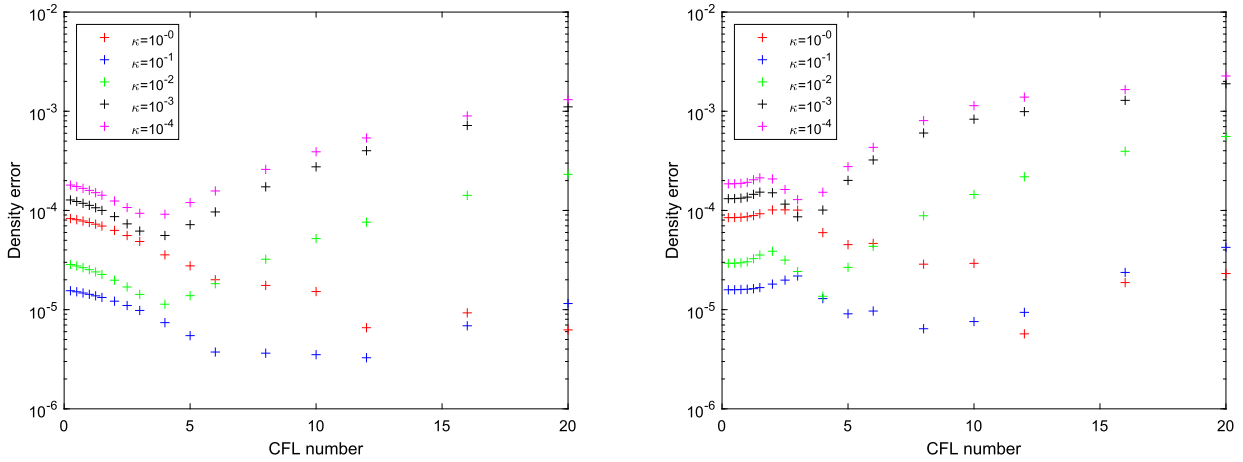

(a) RK3-QCWENO23 (b) BDF3-QCWENO23

Fig. 12. Error versus CFL number. Initial data is given in (54).

6.4.2. 1D Riemann problem

Here we consider the classical Riemann problem to check the shock capturing capability of high order conservative semi-Lagrangian schemes in the fluid limit $\kappa \to 0$. We compare our scheme with non-conservative semi-Lagrangian schemes [5] and with conservative correction based semi-Lagrangian methods [14]. As initial data we consider local Maxwellians with piecewise constant macroscopic quantities used in [5]:

$$(\rho_0, u_0, p_0) = \left\{ \begin{array}{ll} (2.25, 0, 1.125), & \text{for } x \le 0.5 \\ (3/7, 0, 1/6), & \text{for } x > 0.5 \end{array} \right\}. \tag{55}$$

We impose free flow boundary condition on the interval $x \in [0, 1]$, and velocity domain $v \in [-10, 10]$ up to final time $t_f = 0.16$. We take uniform grids with $N_x = 200$, $N_v = 30$ and CFL = 2, which means a time step by $\Delta t = \Delta x/5$. For this test, we use (26), described in Section 4.3.2, to construct the local discrete Maxwellian, which we prefer to the approach based on L^2 minimization, because it guarantees the positivity of local Maxwellian with relatively small number of velocity grid points $N_v = 30$, for which the approach in (23) may produce negative values, thus leading to instability. In Fig. 13, the results obtained with BDF3 scheme are plotted for comparison. The results show that our conservative scheme captures the exact shock position, while non conservative semi-Lagrangian schemes produced shocks with incorrect speed. In Fig. 13d, it appears that conservative solutions converge to the exact solution as we increase the number grid points. This asymptotic convergence behaviour can be also observed in Fig. 13e.

6.5. 2D BGK model

In 2D problem $(d_x, d_v) = (2, 2)$, we take uniform meshes both in space ($\Delta x = \Delta y$) and in velocity ($\Delta v_x = \Delta v_y = \Delta v$). For the BGK model, we use the CFL number defined by

$$\text{CFL} := \max_{1 \le \ell \le d_v} \max_j |v_j^{(\ell)}| \frac{\Delta t}{\Delta x}. \tag{56}$$

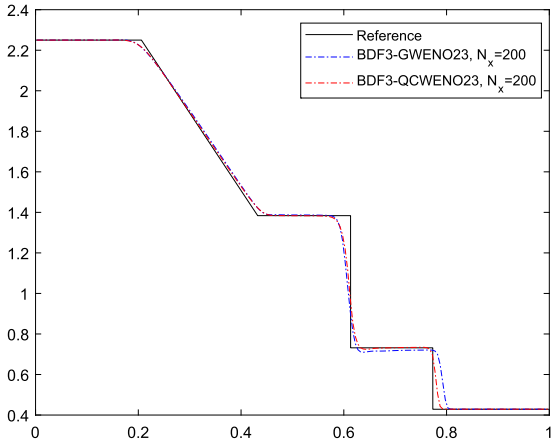

(a) Density

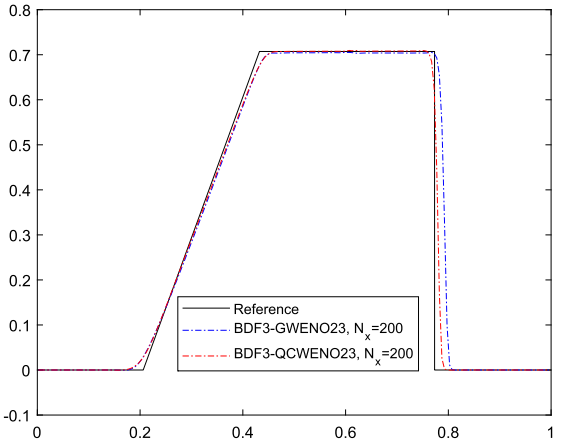

(b) Velocity

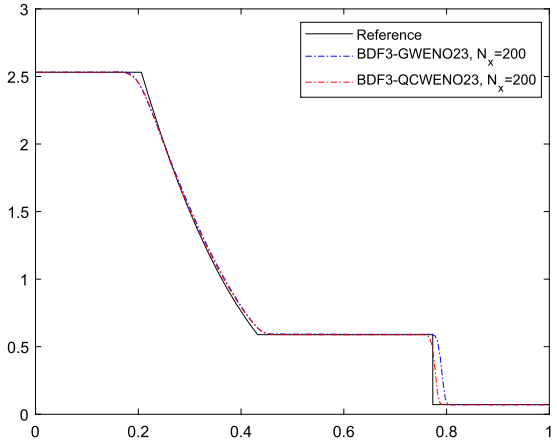

(c) Pressure

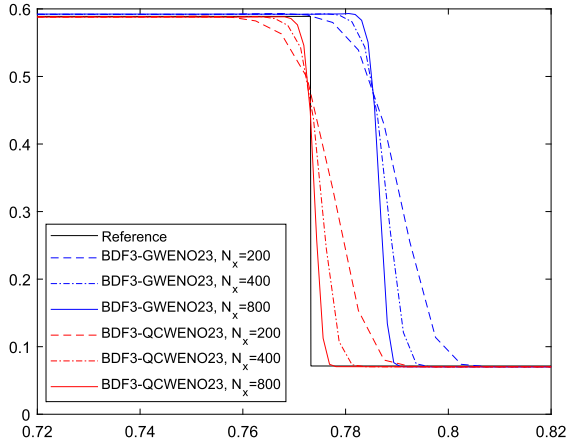

(d) Pressure

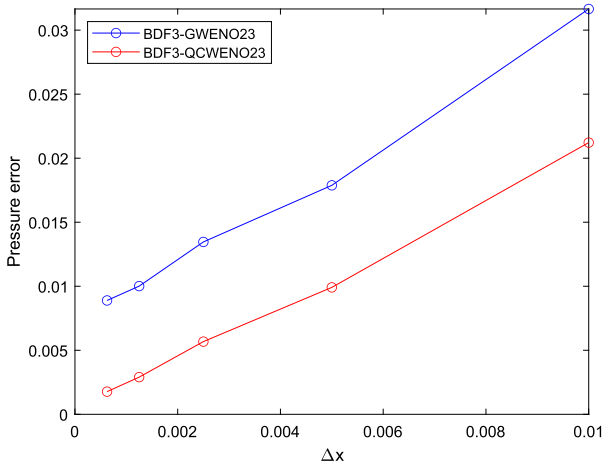

(e) Relative L^1 error in pressure.

Fig. 13. Riemann problem for the 1D BGK model with $\kappa = 10^{-6}$. BDF3 based method with QCWENO23. Initial data is given in (55).

Table 13
Accuracy test for the 2D BGK equation. Initial data is given in (57).

Relative L^1 error and order of density									
Scheme	$(N_x^2, (2N_x)^2)$	$\kappa = 10^{-6}$		$\kappa = 10^{-4}$		$\kappa = 10^{-2}$		$\kappa = 10^{-0}$	
		Error	Rate	Error	Rate	Error	Rate	Error	Rate
RK3	$(40^2, 80^2)$	5.39e-04	2.53	5.13e-04	2.58	8.71e-05	2.70	1.74e-05	3.03
	$(80^2, 160^2)$	9.31e-05	2.63	8.57e-05	2.70	1.34e-05	2.66	2.14e-06	3.02
	$(160^2, 320^2)$	1.50e-05		1.32e-05		2.12e-06		2.64e-07	
BDF3	$(40^2, 80^2)$	7.18e-04	2.34	6.94e-04	2.37	1.35e-04	2.68	2.74e-05	3.03
	$(80^2, 160^2)$	1.42e-04	2.92	1.35e-04	2.94	2.11e-05	2.89	3.36e-06	3.02
	$(160^2, 320^2)$	1.87e-05		1.75e-05		2.84e-06		4.15e-07	

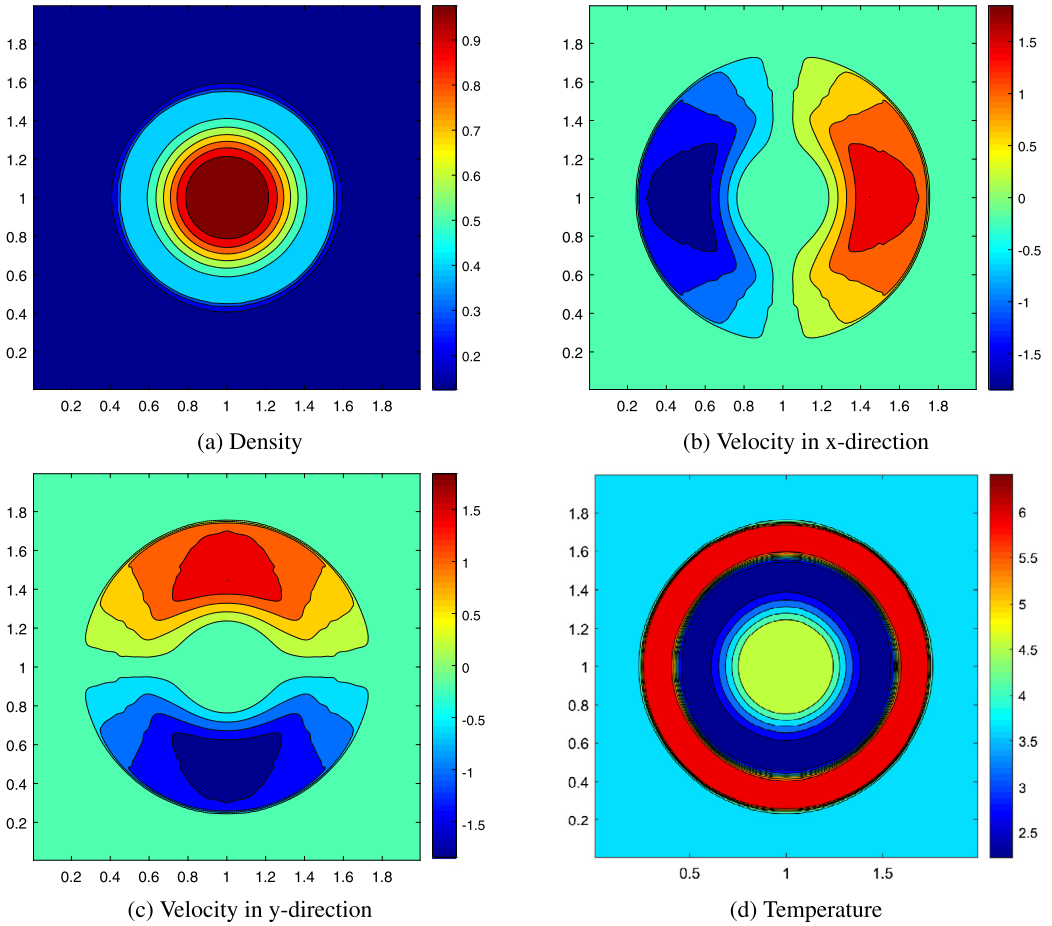

(a) Density (b) Velocity in x-direction

(c) Velocity in y-direction (d) Temperature

Fig. 14. 2D Riemann problem with $\kappa = 10^{-4}$, macroscopic moments.

6.5.1. Accuracy test

Here, we check the accuracy of semi-Lagrangian methods for the 2D BGK model. Initial conditions are taken by the local Maxwellian with the macroscopic quantities:

$$\rho_0(x, y) = 1 + (\sin \pi x)^2 (\sin \pi y)^2, \quad u_0(x, y) = (0, 0), \quad T_0(x, y) = 1, \tag{57}$$

where periodic boundary conditions are imposed on $[0, 1]^2$. We take $N_v = 32$ for the velocity domain $[-10, 10]^2$, which means that we use $(32 + 1)^2$ grid points. The final time is $t^f = 0.6$ up to which the solution remains smooth. We use a fixed time step Δt with CFL $= 4$ using (56). In this test, the positivity of Maxwellian is not strictly demanded, hence, we compute the Maxwellian using (23). Here we consider RK3 and BDF3 based semi-Lagrangian schemes combined with the conservative reconstruction based on the 2D CWENO23 method, so the expected convergence rates are between 2 and 3. Note that 2D CWENO23 is a genuinely 2D reconstruction, so we do not consider dimension by dimension interpolation here.

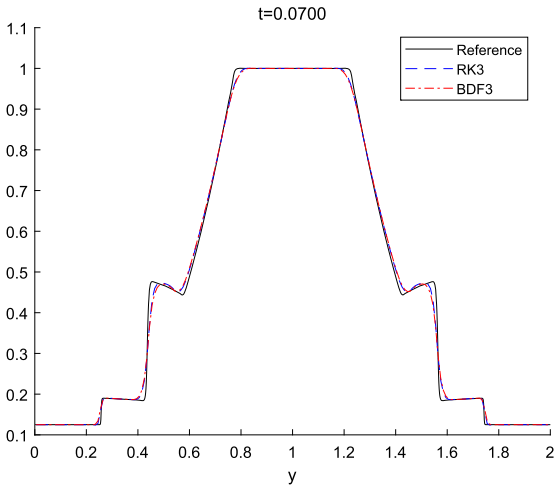

(a) Density

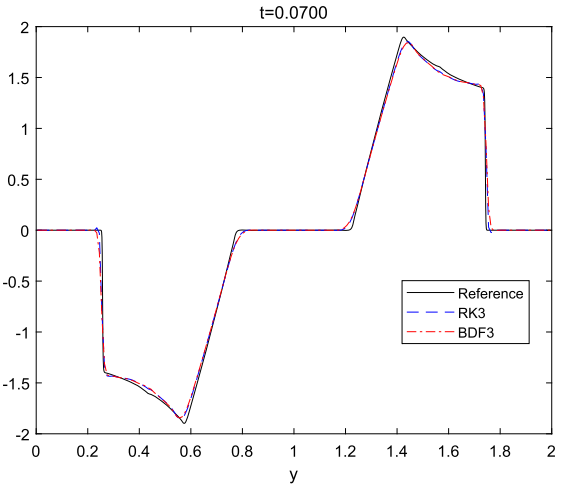

(b) Velocity in y-direction

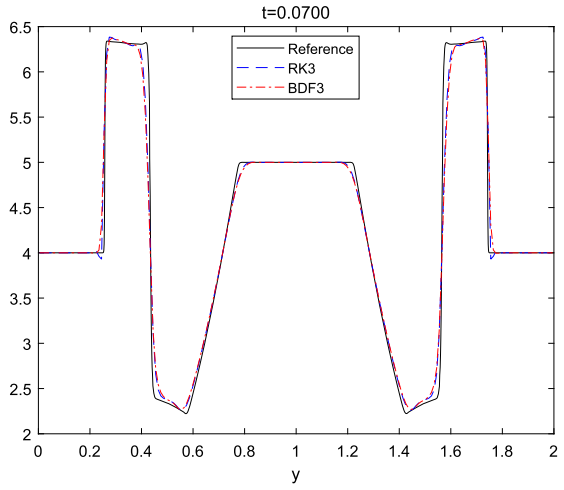

(c) Temperature

Fig. 15. Riemann problem for the 2D BGK model with $\kappa = 10^{-4}$. Macroscopic moments at $x = x_{100}$.

In Table 13, we report the numerical errors and the corresponding accuracy orders for density. The result of BDF3 scheme shows the desired convergence rate 3 for all values of Knudsen number. On the other hand, in case of RK3 method, we observe order reduction in the limit $\kappa = 10^{-6}$ as in the 1D accuracy test (see Table 12). A similar result can be found, for example, in [5].

6.5.2. 2D Riemann problem

Now, we perform a test on the 2D Riemann problem presented in [51]. We use $\kappa = 10^{-4}$ so that the solution is rather close to a local Maxwellian. The initial distribution function is a local Maxwellian with macroscopic moments:

$$(\rho_0, u_{10}, u_{20}, T_0) = \left\{ \begin{array}{ll} (1,0,0,5), & \text{for } (x-1)^2 + (y-1)^2 \le 0.2 \\ (0.125,0,0,4), & \text{for } (x-1)^2 + (y-1)^2 > 0.2 \end{array} \right\}.$$

The computation is performed on the space domain $[0,2]^2$ with free flow boundary conditions; the velocity domain is $[-15,15]^2$, and the final time $t_f = 0.07$. We take uniform grids with $N_x = 200$, $N_y = 200$, and $N_v = 20$ and fix a time step Δt with CFL $= 2.1$ using (56). Here we use the correction to the Maxwellian according to the L^2-projection method, (23).

In Fig. 14, we present a contour plot of the macroscopic variables obtained by the BDF3-QCWENO23 method. In the following Fig. 15, we compare the results obtained by BDF3-QCWENO23 and RK3-QCWENO23 schemes with a reference solution obtained by solving compressible 2D Euler equations by explicit conservative finite difference method with WENO23 and RK3 (with a grid of 1600×1600 points). For comparison, all solutions are plotted at the location $x = 1$. In particular, we plot solution at $x = x_{100}$ which is the closest grid point to $x = 1$. The result shows that high order conservative schemes are

able to capture correct shock positions which appear near $y \approx 0.26$ and $y \approx 1.74$, and reproduce the profile of the reference solution. We omit the figure for the slice of x-directional velocity because the x-directional velocity is zero at $x = 1$, by symmetry.

7. Conclusions

The conservative reconstruction, $Q[u^n]$ derived and analysed in the first part of this paper [1] has been adopted to propose new conservative semi-Lagrangian schemes, which are then applied to a variety of problems, such as the rigid rotation, the Vlasov-Poisson system, and the BGK model.

Q is obtained by sliding average of a basic reconstruction, R, therefore it inherits the properties of R, such as, for example, non-oscillatory behaviour or positivity. The choice of R depends on the properties one would like to maintain for Q.

High order operator splitting is adopted in the case of the rigid rotation and the Vlasov-Poisson system, while no splitting is necessary to solve the BGK model.

The resulting schemes are stable, i.e. they allow large time steps with no CFL restriction, and are high order accurate both in space and time.

In the case of the BGK model, strict conservation is obtained by combining the conservative reconstruction with a conservative treatment of the collision term (which is obtained either using a discrete Maxwellian or a least-square conservative projection). The implicit treatment of the collision term, together with the strict conservation properties of the method, guarantee asymptotic preserving property: as the Knudsen number vanishes, the method becomes a high resolution shock capturing scheme for the underlying Euler equations.

We plan to extend the method to a wider range of problems, including BGK models for polyatomic gases and mixtures, and to analyse in greater detail the resulting limit schemes for compressible Navier-Stokes and Euler equations. Another important issue concerns adaptivity in velocity: regions with small values of the Knudsen number require fewer grid points in velocity. All these issues will be subject of future investigation.

Declaration of competing interest

The authors declare that they have no known competing financial interests or personal relationships that could have appeared to influence the work reported in this paper.

Acknowledgements

We would like to express our deepest gratitude to the editor and unknown reviewers for all the invaluable comments, advices and suggestions, due to which the quality, clarity and readability of the manuscript has greatly improved.

S.Y. Cho has been supported by ITN-ETN Horizon 2020 Project ModCompShock, Modeling and Computation on Shocks and Interfaces, Project Reference 642768. S.-B. Yun has been supported by Samsung Science and Technology Foundation under Project Number SSTF-BA1801-02. All the authors would like to thank the Italian Ministry of Instruction, University and Research (MIUR) to support this research with funds coming from PRIN Project 2017 (No. 2017KKJP4X entitled *Innovative numerical methods for evolutionary partial differential equations and applications*). S. Boscarino has been supported by the University of Catania (*Piano della Ricerca 2016/2018, Linea di intervento 2*). S. Boscarino and G. Russo are members of the INdAM Research group GNCS.

References

[1] S.Y. Cho, S. Boscarino, G. Russo, S.-B. Yun, Conservative semi-Lagrangian schemes for kinetic equations - Part I: reconstruction, J. Comput. Phys. 432 (2021) 110159.
[2] N. Crouseilles, M. Mehrenberger, E. Sonnendrücker, Conservative semi-Lagrangian schemes for Vlasov equations, J. Comput. Phys. 229 (2010) 1927–1953.
[3] V. Grandgirard, M. Brunetti, P. Bertrand, N. Besse, X. Garbet, P. Ghendrih, G. Manfredi, Y. Sarazin, O. Sauter, E. Sonnendrücker, et al., A drift-kinetic semi-Lagrangian 4D code for ion turbulence simulation, J. Comput. Phys. 217 (2006) 395–423.
[4] J.M. Qiu, G. Russo, A high order multi-dimensional characteristic tracing strategy for the Vlasov–Poisson system, J. Sci. Comput. 71 (2017) 414–434.
[5] M. Groppi, G. Russo, G. Stracquadanio, High order semi-Lagrangian methods for the BGK equation, Commun. Math. Sci. 14 (2016) 389–414.
[6] X. K, J.C. Huang, A unified gas-kinetic scheme for continuum and rarefied flows, J. Comput. Phys. 229 (2010) 7747–7764.
[7] G. Dimarco, R. Loubere, J. Narski, Towards an ultra efficient kinetic scheme, Part III: high-performance-computing, J. Comput. Phys. 284 (2015) 22–39.
[8] E. Carlini, R. Ferretti, G. Russo, A weighted essentially nonoscillatory, large time-step scheme for Hamilton–Jacobi equations, SIAM J. Sci. Comput. 27 (2005) 1071–1091.
[9] J.A. Carrillo, F. Vecil, Nonoscillatory interpolation methods applied to Vlasov-based models, SIAM J. Sci. Comput. 29 (2007) 1179–1206.
[10] G. Russo, P. Santagati, A new class of large time step methods for the BGK models of the Boltzmann equation, arXiv:1103.5247, 2011.
[11] P. Santagati, High order semi-Lagrangian schemes for the BGK model of the Boltzmann equation, Ph.D. thesis, Department of Mathematics and Computer Science, University of Catania, 2007.
[12] P.L. Bhatnagar, E.P. Gross, M. Krook, A model for collision processes in gases. Small amplitude process in charged and neutral one-component systems, Phys. Rev. 94 (1954) 511–525.
[13] C. Cercignani, The Boltzmann Equation and its Applications, Springer, New York, 1988.

[14] S. Boscarino, S.-Y. Cho, G. Russo, S.-B. Yun, High order conservative semi-Lagrangian scheme for the BGK model of the Boltzmann equation, Commun. Comput. Phys. 29 (2021) 1–56.
[15] J.-M. Qiu, A. Christlieb, A conservative high order semi-Lagrangian WENO method for the Vlasov equation, J. Comput. Phys. 229 (2010) 1130–1149.
[16] J.M. Qiu, C.W. Shu, Conservative semi-Lagrangian finite difference WENO formulations with applications to the Vlasov equation, Commun. Comput. Phys. 10 (2011) 979–1000.
[17] F. Filbet, E. Sonnendrücker, P. Bertrand, Conservative numerical schemes for the Vlasov equation, J. Comput. Phys. 172 (2001) 166–187.
[18] T. Umeda, Y. Nariyuki, D. Kariya, A non-oscillatory and conservative semi-Lagrangian scheme with fourth-degree polynomial interpolation for solving the Vlasov equation, Comput. Phys. Commun. 183 (2012) 1094–1100.
[19] X. Zhang, C.-W. Shu, On maximum-principle-satisfying high order schemes for scalar conservation laws, J. Comput. Phys. 229 (2010) 3091–3120.
[20] X. Zhang, C.-W. Shu, Maximum-principle-satisfying and positivity-preserving high-order schemes for conservation laws: survey and new developments, Proc. R. Soc. A, Math. Phys. Eng. Sci. 467 (2011) 2752–2776.
[21] D. Levy, G. Puppo, G. Russo, Compact central WENO schemes for multidimensional conservation laws, SIAM J. Sci. Comput. 22 (2000) 656–672.
[22] D. Levy, G. Puppo, G. Russo, Central WENO schemes for hyperbolic systems of conservation laws, Modél. Math. Anal. Numér. 33 (1999) 547–571.
[23] G. Capdeville, A central WENO scheme for solving hyperbolic conservation laws on non-uniform meshes, J. Comput. Phys. 227 (2008) 2977–3014.
[24] I. Cravero, G. Puppo, M. Semplice, G. Visconti, CWENO: uniformly accurate reconstructions for balance laws, Math. Comput. 87 (2017) 1689–1719.
[25] J. Friedrich, O. Kolb, Maximum principle satisfying CWENO schemes for nonlocal conservation laws, SIAM J. Sci. Comput. 41 (2019) A973–A988.
[26] C. F, N. Crouseilles, E. Faou, M. Mehrenberger, High-order Hamiltonian splitting for the Vlasov–Poisson equations, Numer. Math. 135 (2017) 769–801.
[27] H. Yoshida, Construction of higher order symplectic integrators, Phys. Lett. A 150 (1990) 262–268.
[28] L. Mieussens, Discrete velocity model and implicit scheme for the BGK equation of rarefied gas dynamics, Math. Models Methods Appl. Sci. 10 (2000) 1121–1149.
[29] S. Boscarino, S.Y. Cho, G. Russo, S.-B. Yun, Convergence estimates of a semi-Lagrangian scheme for the ellipsoidal BGK model for polyatomic molecules, arXiv:2003.00215, 2020.
[30] G. Russo, S.-B. Yun, Convergence of a semi-Lagrangian scheme for the ellipsoidal BGK model of the Boltzmann equation, SIAM J. Numer. Anal. 56 (2018) 3580–3610.
[31] G. Russo, P. Santagati, S.-B. Yun, Convergence of a semi-Lagrangian scheme for the BGK model of the Boltzmann equation, SIAM J. Numer. Anal. 50 (2012) 1111–1135.
[32] D.R. Nicholson, Introduction to Plasma Theory, Wiley, New York, 1983.
[33] M. Groppi, G. Russo, G. Stracquadanio, Boundary conditions for semi-Lagrangian methods for the BGK model, Commun. Appl. Ind. Math. 3 (2016) 138–164.
[34] F. Filbet, G. Russo, Semilagrangian schemes applied to moving boundary problems for the BGK model of rarefied gas dynamics, Kinet. Relat. Models 2 (2009) 231–250.
[35] I. Gamba, S.H. Tharkabhushaman, Spectral-Lagrangian based methods applied to computation of non-equilibrium statistical states, J. Comput. Phys. 228 (2009) 2012–2036.
[36] A. Frezzotti, Numerical study of the strong evaporation of a binary mixture, Fluid Dyn. Res. 8 (1991) 175.
[37] V. Aristov, F. Tcheremissine, The conservative splitting method for solving the Boltzmann equation, USSR Comput. Math. Math. Phys. 1 (1980) 208–225.
[38] E. Hairer, G. Warner, Solving Ordinary Differential Equations II: Stiff and Differential-Algebraic Problems, Springer, Berlin, 1996.
[39] R.I. McLachlan, G.R.W. Quispel, Splitting methods, Acta Numer. 11 (2002) 341–434.
[40] E. Hairer, G. Warner, S.P. Nòrsett, Solving Ordinary Differential Equations I: Nonstiff Problem, Springer, Berlin, 1996.
[41] J. Hu, R. Shu, X. Zhang, Asymptotic-preserving and positivity-preserving implicit-explicit schemes for the stiff BGK equation, SIAM J. Numer. Anal. 56 (2018) 942–973.
[42] O. Kolb, On the full and global accuracy of a compact third order WENO scheme, SIAM J. Numer. Anal. 52 (2014) 2335–2355.
[43] J.-M. Qiu, C.-W. Shu, Positivity preserving semi-Lagrangian discontinuous Galerkin formulation: theoretical analysis and application to the Vlasov–Poisson system, J. Comput. Phys. 230 (2011) 8386–8409.
[44] I. Cravero, G. Puppo, M. Semplice, G. Visconti, Cool WENO schemes, Comput. Fluids 169 (2018) 71–86.
[45] F. Filbet, E. Sonnendrücker, Comparison of Eulerian Vlasov solvers, Comput. Phys. Commun. 150 (2001) 247–266.
[46] J.A. Rossmanith, D.C. Seal, A positivity-preserving high-order semi-Lagrangian discontinuous Galerkin scheme for the Vlasov–Poisson equations, J. Comput. Phys. 230 (2011) 6203–6232.
[47] G. Russo, J. Qiu, X. Tao, Conservative multi-dimensional semi-Lagrangian finite difference scheme: stability and applications to the kinetic and fluid simulations, J. Sci. Comput. (2018) 1–30.
[48] N. Crouseilles, M. Gutnic, G. Latu, E. Sonnendrücker, Comparison of two Eulerian solvers for the four-dimensional Vlasov equation: part II, Commun. Nonlinear Sci. Numer. Simul. 13 (2008) 94–99.
[49] S. Pieraccini, G. Puppo, Implicit-explicit schemes for BGK kinetic equations, J. Sci. Comput. 32 (2007) 1–28.
[50] M. Falcone, R. Ferretti, Semi-Lagrangian Approximation Schemes for Linear and Hamilton-Jacobi Equations, SIAM, Philadelphia, 2014.
[51] G. Dimarco, R. Loubere, Towards an ultra efficient kinetic scheme, Part II: the high order case, J. Comput. Phys. 255 (2013) 699–719.